

University of Virginia

Mechanical & Aerospace Engineering

EXPERIMENTAL INVESTIGATION INTO THE EFFECT OF A
STATIONARY DORSAL FIN FOR MULTIPLE CONFIGURATIONS -
A BIO-INSPIRED PERSPECTIVE

Author:

Vishaal Samir Saraiya

Advisor:

Dr Hilary Bart-Smith

A thesis submitted in partial fulfilment of the requirements for the degree of

Master of Science in

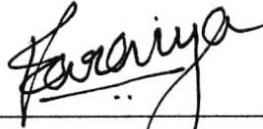
Mechanical and Aerospace Engineering

School of Engineering and Applied Science

May 2017

APPROVAL SHEET

The thesis is submitted in partial fulfilment of the requirements for the degree of
Master of Science in Mechanical and Aerospace Engineering



Vishaal Samir Saraiya

Author

This thesis (or dissertation) has been read and approved by the examining Committee:

Dr Hilary Bart-Smith (Advisor)

Dr Haibo Dong (Chair)

Dr Daniel Quinn

Accepted for the School of Engineering and Applied Science:



Craig H. Benson

Dean, School of Engineering and

Applied Science

Abstract

Results of experiments aimed at determining the performance of two quasi-two-dimensional hydrofoils arranged in an in-line configuration are presented. This thesis aims at understanding the role of pitching motion of a caudal fin in the presence of a dorsal fin, decoupled from heaving motion. A simplified model has been proposed, which accounts for pitching motion, and explores the role of frequency, amplitude, and separation distance between dorsal and caudal fins. The net thrust generated and the work done by the 2-fin model while undergoing prescribed pitching motions were calculated.

The pitch experiments focus on four parameters to quantify their influence on propulsive performance; (1) frequency, (2) trailing edge amplitude, (3) separation between foils, and (4) flexibility of the fins. The experiments are conducted under both accelerating and free swimming conditions.

It is hypothesized that distance of separation between the static dorsal and pitching caudal fins during free swimming will affect the work done and economy across amplitudes and frequencies due to the weakening of the wake from the leading hydrofoil. It is also expected that the change in flexibility at free-swimming speeds will cause a change in economy, and that the presence of the dorsal fin will amplify this effect. Finally, the thrust is hypothesized to follow trends similar to that of a pitching hydrofoil in terms of amplitude and frequency.

While the increased drag due to the additional hydrofoil reduces the speed of motion, it also reduces the required work to move the lagging hydrofoil. The reduction in speed is $\sim 10\%$,

while the required work decreases by $>20\%$ on average, leading to an increase in economy.

The effects increase with increasing amplitude and frequency during acceleration. As the distance between the hydrofoils is increased the efficiency and economy of the model reduces. Finally, flexible foils are more efficient in the presence of a stationary fin only at high frequencies and amplitudes.

This study is a valuable preliminary work towards the evolution of design of bio-inspired models and possibly vehicles.

A secondary aim of this thesis is the development of an inexpensive PIV technique to quantify flow fields. A PIV setup has been designed and built that allows the quantification of flows at speeds below 25.4 cm/s. At greater speeds, error margins exceed 10%.

Acknowledgements

I would like to express my gratitude to my advisor, Dr Hilary Bart-Smith for granting me the opportunity to work under her guidance.

I would also like to thank my colleagues in the lab for their help in building the experimental setup and the tools for effective data collection, as well as Dr Matthew Reidenbach and Jonathan Stocking for their assistance with the setup of the PIV system.

Lastly, I would like to thank my family for their invaluable and steadfast support.

Table of Contents

Abstract.....	i
Acknowledgements	iii
List of Figures	vi
List of Tables	x
List of Symbols	x
Definitions.....	xi
Chapter 1: Introduction.....	1
1.1 Motivation.....	1
1.2 Literature Review	4
1.2.1 Swimming mechanisms of fishes	4
1.2.2 Experimental studies looking at simulating fish movements.....	7
1.2.3 Review of the PIV techniques	11
1.3 Concluding remarks	13
Chapter 2: Experimental Setup	15
2.1 The experimental setup for the hydrofoils.....	15
2.2 PIV Setup.....	26
2.3 Experimental Procedure and Data Analysis:	30
2.3.1 The effect of amplitude and frequency of oscillation, distance of separation, and flexibility of the foil under free swimming conditions:	30
2.3.2 The effect of amplitude and frequency of oscillation of the foil under acceleration:	30
2.3.3 Data analysis.....	31
Chapter 3: Results	33
3.1 Experiment Set 1 - Effect of amplitude and frequency during acceleration on thrust, work done and efficiency.....	36
3.2 Experiment Set 2 - Effect of distance between hydrofoils during acceleration on work done.....	40
3.3 Experiment Set 3 - Effect of distance between hydrofoils and frequency of oscillation during free swimming on swimming speed, work done and economy.....	43
3.4 Experiment Set 4 - Effect of flexibility of oscillating hydrofoil on free swimming speed, work done and economy	47

3.5 Error analysis.....	53
Chapter 4: PIV Setup Validation and Analysis	56
4.1 Validation.....	56
4.2 System advantages and limitations	61
Chapter 5: Conclusions and Discussion	63
Chapter 6: Future Work	70
Chapter 7: Bibliography.....	72

List of Figures

Figure 1.1: Dorsal fins a) Orca b) Rainbow trout c) Ocean Sunfish d) Various types of dorsal fins seen in nature	2
Figure 2.1: Water Tunnel (Source: [65])	16
Figure 2.2: Shows the attachment of the torque sensor to the bottom of the motor, along with the coupling to attach the hydrofoil	17
Figure 2.3: Schematic of Experimental Rig (From left to right: 1. Single hydrofoil configuration 2. Double hydrofoil configuration). Figures are based on [47]	18
Figure 2.4: Schematic of Experimental Rig with Air Bearings and Steel Rods. Figures are based on [47]	18
Figure 2.5: Experimental Rig	18
Figure 2.6: Air bearing floating on the steel rod and pressure gauge	19
Figure 2.7: From left to right: 1) Part B holding the stationary hydrofoil 2) Part B inserted into Part A	20
Figure 2.8: a) Flexible hydrofoil b) Double fin configuration schematic c) double fin configuration d) attachment of Parts A and B to experimental rig	22
Figure 2.9: Schematic of Experimental Data Flow/Protocol	23
Figure 2.10: Ensuring a horizontal plane	27
Figure 2.11: Resulting laser plane	27
Figure 2.12: From left to right 1) PIV Setup 2) PIV Setup Schematic	28
Figure 3.1: Ratio of thrust produced for double hydrofoil to single hydrofoil configuration at a given amplitude v /s frequency when the speed of oncoming flow is 7.62 cm/s. Each curve represents a given amplitude of oscillation, whose half sweep values are noted as legends.	36
Figure 3.2: Ratio of thrust produced for double hydrofoil to single hydrofoil configuration at a given amplitude v /s frequency when the speed of oncoming flow is 10.16 cm/s. Each curve represents a given amplitude of oscillation, whose half sweep values are noted as the legends.	37

Figure 3.3: Ratio of work done for double hydrofoil to single hydrofoil configuration at a given amplitude v/s frequency when the speed of oncoming flow is 7.62 cm/s. Each curve represents a given amplitude of oscillation, whose half sweep values are noted as the legends.

38

Figure 3.4: Ratio of work done for double hydrofoil to single hydrofoil configuration at a given amplitude v/s frequency when the speed of oncoming flow is 10.16 cm/s. Each curve represents a given amplitude of oscillation, whose half sweep values are noted as the legends.

38

Figure 3.5: Ratio of efficiency for double hydrofoil to single hydrofoil configuration at a given amplitude v/s frequency when the speed of oncoming flow is 7.62 cm/s. Each curve represents a given amplitude whose values are noted as legends.

39

Figure 3.6: Ratio of efficiency for double hydrofoil to single hydrofoil configuration at a given amplitude v/s frequency when the speed of oncoming flow is 10.16 cm/s. Each curve represents a given amplitude whose values are noted as legends.

39

Figure 3.7: Ratio of work done for double hydrofoil configuration to single hydrofoil configuration at a given speed (7.62 cm/s), amplitude (20 degrees) and frequency of oscillation v/s distance of separation. Each curve represents a given frequency of oscillation whose values are denoted as legends.

41

Figure 3.8: Ratio of work done for double hydrofoil configuration to single hydrofoil configuration at a given speed (10.16 cm/s), amplitude (20 degrees) and frequency of oscillation v/s distance of separation. Each curve represents a given frequency of oscillation whose values are denoted as legends.

41

Figure 3.9: Ratio of work done for double hydrofoil to single hydrofoil configuration at a given amplitude (20 degrees) v/s frequency when the speed of oncoming flow is 7.62 cm/s. Each curve represents a given distance of separation whose values are noted as legends.

42

Figure 3.10: : Ratio of work done for double hydrofoil to single hydrofoil configuration at a given amplitude (20 degrees) v/s frequency when the speed of oncoming flow is 10.16 cm/s. Each curve represents a given distance of separation whose values are noted as legends.

42

Figure 3.11: Ratio of speeds of double hydrofoil to single hydrofoil configuration at a given amplitude (20 degrees) v/s frequency under free swimming conditions. Each curve represents a given distance of separation whose values are noted as legends.

44

Figure 3.12: Ratio of work done of double hydrofoil to single hydrofoil configuration at a given amplitude (20 degrees) v/s frequency under free swimming conditions. Each curve represents a given distance of separation whose values are noted as legends.

44

Figure 3.13: Ratio of economy for double hydrofoil to single hydrofoil configuration at a given amplitude (20 degrees) v/s frequency under free swimming conditions. Each curve represents a given distance of separation whose values are noted as legends.

44

Figure 3.14: Ratio of speeds of double hydrofoil to single hydrofoil (flexible) configuration at given amplitude (20 degrees) v/s frequency. Each curve represents a given distance of separation whose values are noted as legends. _____48

Figure 3.15: Ratio of work done of double hydrofoil to single hydrofoil (flexible) configuration at given amplitude (20 degrees) v/s frequency. Each curve represents a given distance of separation whose values are noted as legends. _____48

Figure 3.16: Ratio of efficiencies of double hydrofoil to single hydrofoil (flexible) configuration at given amplitude (20 degrees) v/s frequency. Each curve represents a given distance of separation whose values are noted as legends. _____48

Figure 3.17: Ratio of free-swimming speeds for both rigid and flexible double fin configurations to their corresponding single fin configurations at a given amplitude (20 degrees) v/s frequency. Each curve represents a given type of hydrofoil and a given distance of separation whose values are noted as legends (RH – Rigid hydrofoil, FH – Flexible Hydrofoil). _____50

Figure 3.18: Ratio of work done for both rigid and flexible double fin configurations to their corresponding single fin configurations at a given amplitude (20 degrees) v/s frequency. Each curve represents a given type of hydrofoil and a given distance of separation whose values are noted as legends (RH – Rigid hydrofoil, FH – Flexible Hydrofoil). _____51

Figure 3.19: Ratio of economy for both rigid and flexible double fin configurations to their corresponding single fin configurations at a given amplitude (20 degrees) v/s frequency. Each curve represents a given type of hydrofoil and a given distance of separation whose values are noted as legends (RH – Rigid hydrofoil, FH – Flexible Hydrofoil). _____51

Figure 3.20: Ratio of speeds of double hydrofoil to single hydrofoil configuration at a given amplitude (20 degrees) v/s frequency under free swimming conditions. Each curve represents a given distance of separation whose values are noted as legends. _____54

Figure 3.21: Ratio of speeds of (flexible) double hydrofoil to single hydrofoil configuration at a given amplitude (20 degrees) v/s frequency under free swimming conditions. Each curve represents a given distance of separation whose values are noted as legends. _____55

Figure 4.1: Sample consecutive images before processing. The area with the hydrofoil is masked while processing. _____58

Figure 4.2: Velocity profile for consecutive images shown in Figure 4.1 without interpolation _____59

Figure 4.3: Velocity profile for consecutive images shown in Figure 4.1 without interpolation - zoomed in _____59

Figure 4.4: Velocity profile for consecutive images shown in Figure 4.1 _____60

Figure 5.1: Samples images under consideration _____ 66

Figure 5.2: Time averaged magnitude of velocity of flow behind the stationary hydrofoil.
Both axes are in cm. The colour bar shows the magnitude of velocity in cm/s. _____ 67

Figure 5.3: Cross-sectional time averaged velocity profile of flow at a given distance behind
the stationary hydrofoil. The x axis represents distance perpendicular to the flow direction. 68

List of Tables

<i>Table 1: Definitions.....</i>	<i>xii</i>
<i>Table 2: Parameter Domains and Units</i>	<i>21</i>
<i>Table 3: Key for figure 2.7</i>	<i>23</i>
<i>Table 4: Range of parameter values for experiment sets</i>	<i>33</i>
<i>Table 5: Parameter Space for Experimental Sets and Repetitions</i>	<i>34</i>

List of Symbols

ω	Angular Velocity
η	Efficiency
η'	Economy
μ	Micro
St	Strouhal Number
A	Half sweep amplitude in terms of degrees
A'	Peak to peak amplitude in terms of distance, measured at the tip of the hydrofoil
f	Frequency
S	Swimming speed
R	Number of repetitions of test
D	Distance of separation between leading edges of leading and lagging hydrofoil

Definitions

Term	Definition
Single hydrofoil configuration	A single hydrofoil connected to the motor and torque sensor.
Double hydrofoil configuration	A single hydrofoil connected to the motor and torque sensor with a stationary hydrofoil in front of it, parallel to the direction of flow, at a given distance
Leading hydrofoil	The first hydrofoil in the double hydrofoil configuration which is always stationary with its mean chamber line parallel to the direction of flow. It is always rigid.
Lagging hydrofoil	The second hydrofoil in the double hydrofoil configuration which is always undergoing sinusoidal pitching with its mean chamber line parallel to the direction of flow in its initial position. It may be rigid or flexible.
Flexible hydrofoil	This hydrofoil is made of 3d printed material and Dragon Skin® silicone.
Flexible double hydrofoil configuration	A flexible lagging hydrofoil and a rigid leading hydrofoil
Distance of separation	Distance between leading edge of lagging hydrofoil and leading edge of leading hydrofoil
Work Done	The product of the instantaneous torque and angular velocity averaged over time.

Efficiency	The ratio of thrust generated to the work done
Economy	The ratio of free-swimming speed to the work done
Neutral position	Position at which the experimental rig settles on the guideways (steel rods) after given a small disturbance.

Table 1: Definitions

Chapter 1: Introduction

1.1 Motivation

With the increasing importance given to autonomous vehicles and robots, underwater vehicles have received increased attention. Their applications now range across several industries, and involve survey, exploration, inspection, and research. Most of these vehicles have conventionally been designed with rigid bodies and rotating propellers that utilize steady hydrodynamics. In contrast, biological swimmers use their flexible bodies and take advantage of unsteady hydrodynamics and oscillatory motions to generate thrust.

Conventional rigid hull designs involving propellers have several disadvantages including excessive noise, limited accelerations, and large, easily detectable wakes. They are efficient in terms of energy only under specific operating conditions, or have low manoeuvrability. In contrast, biological swimmers have evolved over millennia resulting in efficient swimming mechanisms, with natural selection ensuring the presence of characteristics like manoeuvrability, high speeds, and quick accelerations with low energy consumption. As a result, biological swimmers are much more manoeuvrable and efficient when compared to conventional vehicles.

It is this that motivates the development of biologically inspired designed platforms. The diversity of the animal kingdom grants us a vast array of sources from which to draw inspiration. There is an increasing interest in biologically inspired designs, to leverage the advantages both their shape and their flexible bodies offer. Focused on the goal of furthering the understanding the effects of fins in tandem, this study looks at the effect of a stationary

hydrofoil held in-line with an oscillating one (pure pitching). Figure 1.1 shows multiple examples of this configuration and its variants in terms of size and shape, as seen in nature.

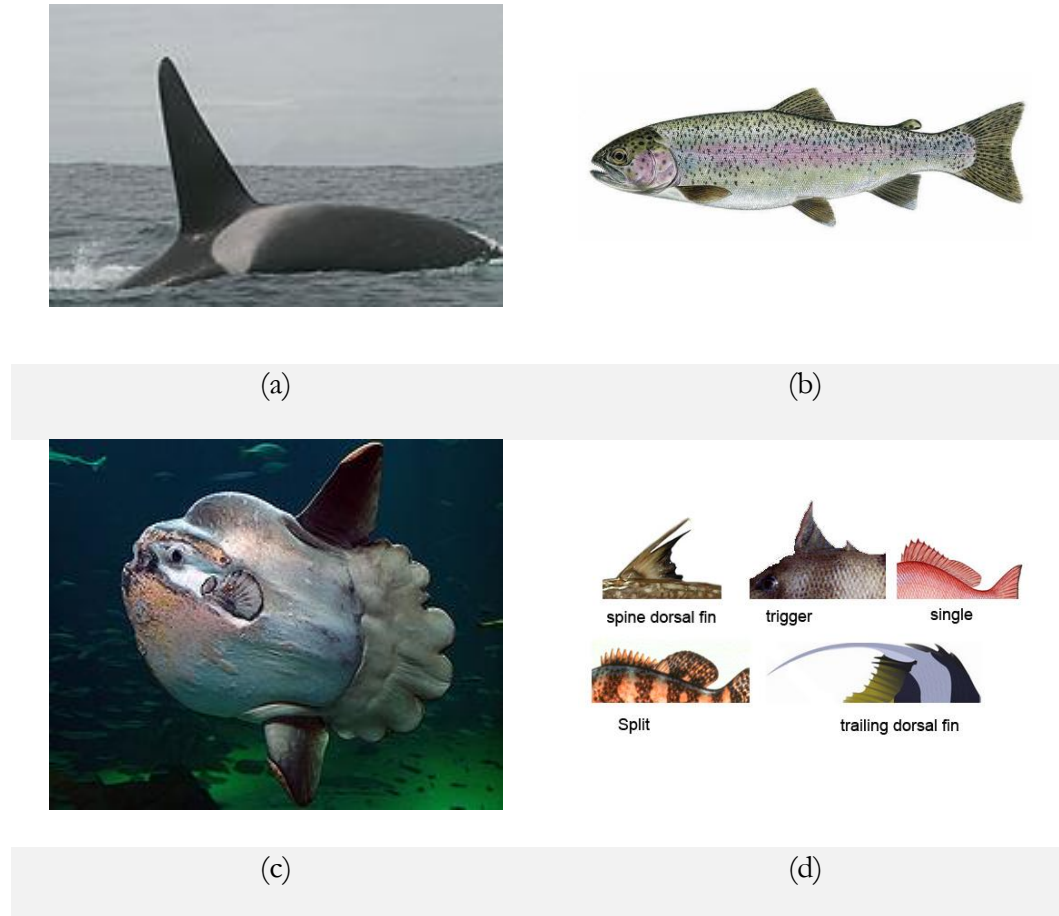


Figure 1.1: Dorsal fins a) Orca b) Rainbow trout c) Ocean Sunfish d) Various types of dorsal fins seen in nature

Studies suggest that fish can change their motion and rate of flapping of the caudal fin to take advantage of the surrounding flow, which gives an indication as to the parameters that could be varied during testing for hydrodynamic benefit.

While studies (as shown in the literature review) have looked at the effect of surrounding flows and the hydrodynamics of oscillating fins in tandem, the effect of a stationary dorsal fin has not been explored in much detail. The main evolutionary reason for its existence is stabilizing the body of the fish; this study looks to see if there is any hydrodynamic benefit to it.

To test this hypothesis, the influence of a stationary hydrofoil in front of a purely pitching hydrofoil—representing a simplified model to simulate a dorsal-caudal fin configuration—is experimentally quantified. In this work, hydrofoils are used to simulate the biological fins. A secondary aim of this thesis is the development of an inexpensive and sufficiently robust PIV technique to quantify flow fields. The experimental setup is described in Chapter 2 while the validation tests for and the limitations of the PIV technique are discussed in Chapter 4.

Chapter 3 presents the results of the experiment sets performed to understand the effect of the presence an inline leading stationary hydrofoil on a pitching lagging hydrofoil. The experiments focus on four parameters to quantify their influence on propulsive performance; (1) frequency, (2) trailing edge amplitude, (3) separation between foils, and (4) flexibility of the fins. The experiments are conducted under both accelerating and free swimming conditions.

Chapter 5 summarises the results and conclusions and considers possible areas of interest that could expand upon the work presented in this thesis.

1.2 Literature Review

Extensive experimental and computational studies have generated a great deal of understanding about the swimming mechanisms of fishes. Due to the large body of literature available the literature review has been divided into 3 parts

1. Swimming mechanisms of fishes
2. Experimental studies simulating the swimming mechanisms of fishes
3. Review of the usage of the PIV techniques used in this scenario

1.2.1 Swimming mechanisms of fishes

Fish swim with great agility, and certain species can reach high speeds. The relatively large-amplitude unsteady motion of their bodies is striking and intriguing to the observer. Swimming mechanisms of fishes has been an area of interest for centuries; one of its earlier documentation is in the time of Aristotle. Borelli is claimed to be the next significant contributor. Since then there has been a continued interest in understanding how fish generate thrust to swim, how their structural adaptations help improve efficiency, economy and manoeuvrability, and how their functional adaptations use the oncoming flow to their advantage.

Some of the first studies on basic animal and fish locomotion were carried out by Breder [1], Alexander [2], and Gray [3]. Gray [3] estimated that the muscular power of a dolphin is sevenfold less than the power needed to propel a rigid-straight model of its body at a speed between 15 and 20 knots, which he hypothesized to be the maximum speed achievable by dolphins (Gray's paradox). This generated much interest in the subject of fish locomotion and

in understanding the hydrodynamics of biological propulsion—motivated with trying to validate or disprove Gray’s results.

Initial studies observed the undulation of fish bodies that caused motion, looking at muscle function and movement patterns [4]. Others addressed the subject of fish propulsion. They studied the effect of interaction between the fish's body and the reactive forces from the water and the effect of body structure and movement on thrust [5] [6] [7] [8].

By the beginning of the 21st century, marine propulsion and manoeuvring had already reached a level of maturity. Studies undertaken proved that fishes use the unsteadiness in the surrounding flow to their advantage to generate large short duration forces efficiently, (similar effect observed in bird flapping, especially for high amplitudes [9]) coordinate rhythmic unsteady body and tail motion to minimize the energy required for steady propulsion, and coordinate transient motion of the body and tail to minimize the energy lost in the wake during manoeuvring [8] [10] [11] [12] [13].

Several papers [14] [15] remark on the similarity in movement mechanisms of top predators such as tuna and makos, despite their evolutionary divergence over 400 million years ago. Others note the active control some fishes have over their bodies, allowing them to change fin curvature, area and displacement, and the way they use the same to improve efficiency [16]. Anderson (1996) [8] used experimental digital particle image velocimetry (DPIV) to visualize the wake behind swimming Giant Danio (*Danio malabaricus*) and identified the active manipulation of shed wake vorticity to create a reverse Karman vortex street. Triantafyllou et al. (1996) [17] and others [11] analysed the wake of a swimming mullet using DPIV and concluded that the manipulation of the wake structure resulted in high propulsive efficiencies.

Wolfgang et al. [12] compared experimental DPIV with numerical results. They found that an inviscid numerical formulation provided a good description of the kinematics of the flow around the body and in the wake. A similar methodology was developed and used by Liu and Bose (1997) [18] to treat flexible unsteadily operating foils. While these studies focused on the kinematics of flow around the entire body, others focused on individual fins.

Ahlborn et al. (1991, 1997) [19] [20] showed the flow visualization caused by a rectangular panel forced to move in a ‘double flip’ simulating the caudal fin motion (i.e. motion to one side, shedding a vortex, followed by a reverse-direction motion, shedding a vortex of the opposite sign). This results in the formation of a pair of thrust-producing vortices. These experiments showed that a time lag between flips enhanced thrust production because it allowed for the proper growth of the thrust-producing eddies.

The dorsal fin has received its fair share of attention with studies on understanding the hydrodynamics of the dorsal fin, its effect on stability during turning as well as to compensate for the heaving motion of the caudal fin, and the effect of its stiffness. These studies focus on the change in movement of the dorsal fin as a function of speed [21] [22] [23] and do not consider its influence on the propulsive performance.

While [21] [24], in particular, look at the hydrodynamics of the dorsal fin and explore its effect on force generation, they do not quantify the work done and/or the energy expended. These studies were generally conducted under free-swimming conditions and their approach entailed observing the patterns seen in nature and providing an explanation. This work takes a different approach, as explained in Section 1.2.3.

1.2.2 Experimental studies looking at simulating fish movements

As mentioned previously, fishes use the vortices in the oncoming flow as well as the ones formed due to their body motion, sense and manipulate these vortices as they move down the body, and eventually reposition them through tail motion [25] [26] [27] [28]. Unsteady motion of a body and unsteady forcing in the flow can be used for efficient flow control [29] [30] [31]. The mechanics of flow body interaction are reviewed in Rockwell (1998) [32].

Gursul & Ho (1992) [33] show that unsteady motion of aerofoils can cause a very high lift coefficient and others [34] [35] show that oscillating foils can produce propulsive thrust efficiently. Finally, an oscillating foil can be used to alter oncoming vorticity [36] [37] and recapture energy contained in the eddies.

Thrust is produced when the time-averaged flow downstream of the foil has the form of a jet; Two-dimensional flow studies show that the downstream flow may be characterized by a wake that has either two large or four vortices per period. High propulsive efficiency is associated with the formation of two vortices per cycle, forming a staggered array of vortices resembling a Karman street behind bluff bodies, but with the vortices rotating in opposite directions. Studies [17] [38] proposed that optimum efficiency is obtained when the frequency of foil oscillation coincides with the frequency of disturbances.

Wu (1971a) [39] and others [40] [41] [42] [43] investigated the thrust due to flexible two- and three-dimensional plates by using potential flow theory, following which, the elongated shape of most fishes allowed the slender-body theory to dominate the theoretical modelling of fish hydrodynamics for a time. Flow visualization, however, showed that the flow might differ qualitatively from the flow presumed in slender-body theory. [44]

A significant amount of attention has been given to studying the effect of vortex shedding from a bluff body on swimming mechanisms of fishes, generally simulated using a cylinder. This interest was triggered when fishes were observed to swim in the wakes of boats. This effect is so significant and the motion so distinct from the norm that it has its own name: 'Karman gait'. Liao et al. (2003) [13] studied the unique pattern of axial body motion of trout swimming behind cylinders. They observed that the tail-beat frequency is not only lower than might be expected for a trout swimming in the reduced flow behind a cylinder, but also matches the vortex shedding frequency of the cylinder. Therefore, in addition to choosing to swim in the slower flow velocity offered behind a cylinder, trout are also altering their body kinematics to synchronize with the shed vortices, using a mechanism that may not involve propulsive locomotion. It must be noted that they also show that the bow wake in front of the cylinder was the most energetically favourable region for the fish to hold its position relative to the cylinder, given an oncoming flow. This work has looked at the possibility of a similar mechanism, however it focuses on the vortices shed by dorsal fins rather than cylinders, which reduces the magnitude of circulation of the vortices shed as well as the velocity profile, though alternating vortices are still observed. Liao et al. [13] also observed that fish adjust their kinematics optimally to the shed vortices.

Starting with single foil experiments, Read, Hover, & Triantafyllou (2003) [45] performed experiments on a single foil undergoing pitching and heaving motions. The effect of angle of attack, heave amplitude, phase difference between pitch and heave and Strouhal number was noted. Hover, Haugsdal, & Triantafyllou (2004) [46] noted the effect of changing the above motions from a sinusoidal wave to a square wave, a symmetric sawtooth wave, and a cosine function.

Lauder et al. (2007) [47] advocates the use of bio robotic models as a necessity to further the understanding of aquatic propulsion. They show that the interaction between dorsal and caudal fins can be replicated using pitching panels, which allow the experiments to go beyond the physical constraints on fishes. The paper also reviews different conceptual designs for robotic models of aquatic propulsion. This study draws on the paper as inspiration for using robotic models.

This argument went beyond fishes as Licht et al. (2010) [48] showed experimentally that flapping foil kinematics consisting of a power downstroke and a feathering upstroke together with a properly timed in-line motion, similar to those employed in forelimb propulsion of sea turtles, could produce high thrust and be hydrodynamically as efficient as symmetrically flapping foils.

This study uses the arguments and results presented in the aforementioned publications [47] [48] as well as [49] [50] [51] to justify the use of robotic models and those presented in [47] [16] to justify the use of flapping hydrofoils in lieu of fins. [16] also justifies the use of NACA 0012 hydrofoils as structurally accurate shapes to replace fins.

Clark and Smits (2006) [52] performed experiments to quantify the hydrodynamic performance of a flexible fin inspired by a batoid, evaluating thrust and power consumption to find the optimal efficiency condition and the effect of Strouhal number on wake topology. Thrust was found to increase with non-dimensional frequency, and an optimal oscillatory gait was identified.

Alben et al. (2012) [53] used modelling and simulations guided by initial experiments to study thin foils that were oscillated at the leading edge and were free to move unidirectionally under

the resulting fluid forces. They found resonant-like peaks in the swimming speed as a function of foil length and rigidity.

Lauder, Flammang, and Alben (2012) [54] used simple models of flexing fin bodies under self-propulsion. This model, coupled with experimental data, demonstrates an interesting resonance phenomenon in which swimming speed varies with foil length in an oscillatory manner. Small changes in length can have dramatic effects on swimming speed, and this relationship changes with flexural stiffness of the swimming foil.

Dewey et al. (2013) [55] worked on understanding the hydrodynamics of flexible pitching foils. It was found that flexible panels can give a significant amplification in terms of propulsive efficiency when compared to rigid panels. The global maxima in terms of efficiency was achieved when two conditions are simultaneously satisfied: the oscillation of the panel yields a Strouhal number in the optimal range ($0.25 < St < 0.35$) as found by Triantafyllou, Triantafyllou, and Grosenbaugh (1993) [56] and this frequency of motion is tuned to the structural resonant frequency of the panel. In addition, new scaling laws for the thrust production and power input to the fluid are derived for the rigid and flexible panels.

Finally, Boschitsch et al. (2014) [57] and Dewey et al. (2014) [58] carried out studies to understand the hydrodynamics of hydrofoils pitching in tandem. [57] presents the experimental results for two hydrofoils pitching in tandem in an in-line configuration. The distance between the hydrofoils and the phase difference between the pitching motion of the hydrofoils was varied, with the thrust produced, work done and efficiency were used as metrics for comparison. Under optimal conditions, enhancements of about 50% were observed for the thrust production and propulsive efficiency of the downstream foil, while under other

conditions reductions of about 50% were observed in the same quantities. [58] presents the results of a similar study in which the hydrofoils were in a side-by-side configuration and showed that for in-phase oscillations, the foils exhibit an enhanced propulsive efficiency at the cost of a reduction in thrust while for oscillations at intermediate phase differentials, one of the foils experiences a thrust and efficiency enhancement while the other experiences a reduction in thrust and efficiency.

However, in both these studies [57] [58] both the foils were pitching. Drawing on inspiration from the above, this study attempts to answer the question as to whether the placement of a stationary hydrofoil in front of a pitching hydrofoil offers any advantage in terms of speed/thrust, work done and economy/efficiency.

1.2.3 Review of the PIV techniques

A secondary aim of this thesis is the development of an inexpensive PIV system; this section looks at studies that have used predecessors of the same, as well as the development and use of the open source code implemented to process the images captured.

Reidenbach, George and Koehl (2008) [59] credit Cowen & Monismith (1997) [60] as the basis for the algorithm used to process them images for quantifying flow fields. They assessed the accuracy of the PIV measurements using a separate calibration facility where the camera was towed under a flume at a known speed. The overall accuracy was found to be $\pm 6\%$ of the relative mean velocity.

Reidenbach, George and Koehl (2008) [59] show that the density of the particles used has no measurable effect on velocity calculations. Particles with the same set of specifications have been used in this setup, at similar flow speeds.

Cowen and Monismith (1997) [60] details the hybrid digital particle image velocimetry/particle tracking velocimetry algorithm, which has been implemented in the open source package MatPIV. While the current version has been updated to address compatibility issues, the framework of the algorithm remains the same.

Stocking, Rippe, & Reidenbach (2016) [61] use the same scripts to study the structure and dynamics of turbulent boundary layer flow over healthy and algae-covered corals. Other papers using this technique include [62] [63].

On another note, [64] compared four different softwares for PIV, specifically for hypersonic purposes. MatPIV came in second, with some issues of peak locking, but extremely accurate results beyond that.

1.3 Concluding remarks

Many of the studies are performed under self-propelling conditions and the experiments that look at the effect of dorsal fin assume it to be flexible and/or oscillating/pulsing. They also tend to consider its effect in the presence of the fish's body, which does not isolate its effects and considers a smaller dorsal fin. While these studies are immensely helpful in understanding fish swimming mechanisms, this leaves a gap in terms of quantifying the effect of a stationary dorsal fin on propulsive performance during acceleration and free swimming.

In order to address this gap, the following sets of experiments are proposed which compare the single hydrofoil configuration and double hydrofoil configuration to provide a more holistic view of the effect of the presence of a dorsal fin. To reiterate, the single hydrofoil configuration involves a single hydrofoil oscillating at a given frequency and amplitude, simulating just the caudal fin. The double hydrofoil configuration has two hydrofoils, with the lagging foil undergoing pitching motion, simulating a stationary dorsal fin and a pitching caudal fin.

Experiment sets:

1. Effect of frequency and amplitude during acceleration
2. Effect of distance between hydrofoils during acceleration
3. Effect of distance between hydrofoils during free swimming
4. Effect of flexibility of oscillating hydrofoil during free swimming

An experiment to understand how the correlation of vortex shed from the dorsal fin and caudal fin position during acceleration is also proposed and performed.

The experiments are described in more detail in Chapter 3.

The study aims at quantifying the changes in free swimming speed (thrust generation if testing under acceleration condition), work done and economy (efficiency) to help in the design of future vehicles. This study attempts to understand the biological reason for the existence of the dorsal fin beyond stabilization, and considers the possible benefit of its potential applications in the creating of new artificial setups.

It is hypothesized that the thrust and power consumption follows trends similar to those of a pitching hydrofoil in terms of amplitude and frequency, and that increasing the distance of separation will reduce any effects of the presence of the leading hydrofoil (simulating the dorsal fin), barring the increased drag on the entire setup due to the presence of the second fin. The focus of this work is to see whether a stationary leading hydrofoil can be used to create any benefit in terms of work done and efficiency, as the speed of swimming of the double hydrofoil configuration is expected to be less than or equal to the speed of swimming of a single hydrofoil configuration.

Chapter 2: Experimental Setup

This chapter presents the experimental setup used in the study. It has been split into two parts:

1. Experimental setup for the hydrofoils to study influence of foils in series
2. PIV setup

2.1 The experimental setup for the hydrofoils

In order to test the hypothesis posed in the previous chapter, a custom rig was designed, built and used in conjunction with a water tunnel. The setup allows for testing under free-swimming conditions as well as under acceleration conditions and real data time collection.

This experimental setup consists of a water tunnel, a free moving test platform housing the air tanks and electronics used to control the motion of the hydrofoils described forthwith, the sensors including the load cell and the torque sensor, and the hydrofoils. The platform is referred to as the experimental carriage or the experimental rig.

The water tunnel (Figure 2.1) has a capacity of 1,000 gallons. It has a velocity range from 0 to 31.5 in/s, and a velocity uniformity of $\pm 2\%$ ([65], Rolling Hills Research Corporation®), achieved through a series of upstream flow straighteners. Flow is driven by a 7.5 horsepower centrifugal pump, and the water tunnel is also outfitted with a pressurized 6-color dye system for flow visualization. Schematics for the design and layout of the water tunnel are shown in Fig. 2.1 (www.rollinghillsresearch.com).

ROLLING HILLS RESEARCH
CORPORATION

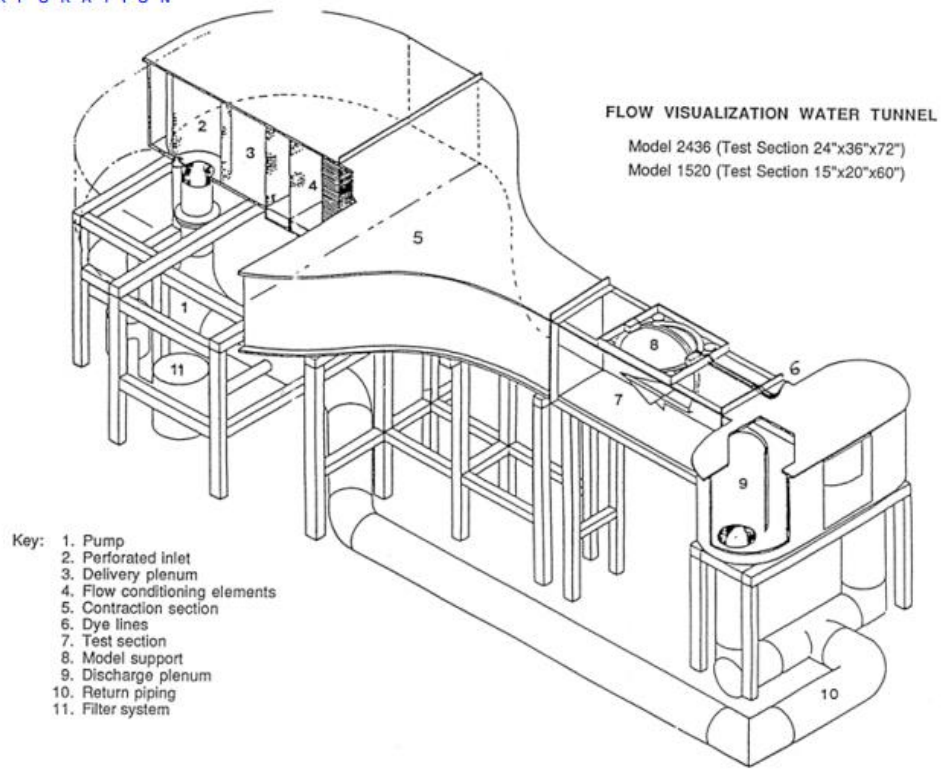


Figure 2.1: Water Tunnel (Source: [65])

The experimental rig (Figure 2.5). is placed on top of the water tank. A large acrylic sheet is used to suppress the surface waves. It has a slit along the middle to allow the hydrofoils connected with the rig to move in the tank. Beams are used to support two steel rods on which two air bearings are free to move, allowing motion parallel to the direction of flow (Figure 2.4, Figure 2.6). The foils are supported by the bearings and are oscillated by a motor (Dynamixel MX-64; Trossen Robotics®). Two small acrylic sheets holding small bearings are placed below the motor at a distance of 5 cm each. The rod holding the (lagging) hydrofoil passes through these sheets before connecting to the torque sensor, fit on the motor, reducing bending in the rod during oscillation of the hydrofoil, and preventing possible heaving motion of the hydrofoil. The diameter of the rod is 5.8 mm.

The torque sensor (TQM202-50; Omega Engineering®; Accuracy $\pm 0.2\%$) is placed directly below the motor, and allows for real time measurement of the torque during testing (Figure 2.2).

The load cell (Low Range Constant Moment Beam Load Cell - LC601-1; Omega Engineering®; Accuracy $\pm 0.03\%$) is placed at the back of the entire rig, in line with the rod of the oscillating hydrofoil, fixed onto the stationary beam that supports the rig. The end of the gauge is rigidly attached to the rod of the oscillating hydrofoil, allowing for rotation of the hydrofoil, but not movement in any other direction.

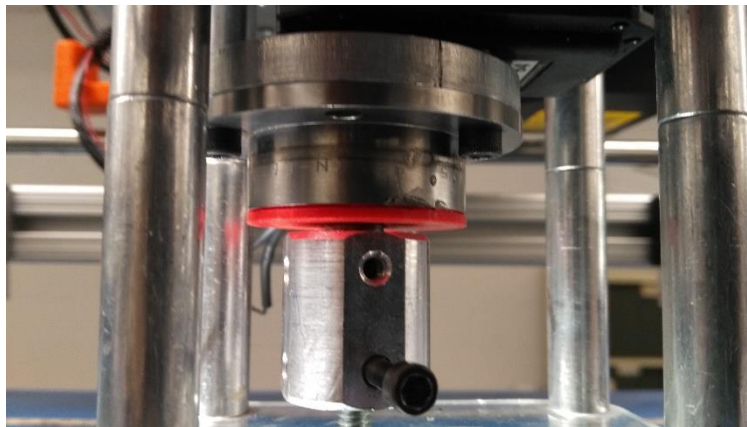


Figure 2.2: Shows the attachment of the torque sensor to the bottom of the motor, along with the coupling to attach the hydrofoil



Figure 2.3: Schematic of Experimental Rig (From left to right: 1. Single hydrofoil configuration 2. Double hydrofoil configuration). Figures are based on [47]

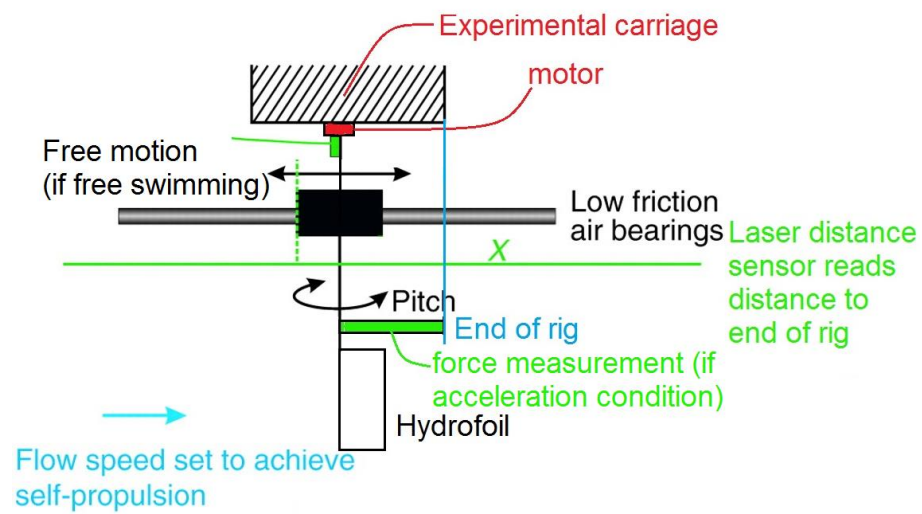


Figure 2.4: Schematic of Experimental Rig with Air Bearings and Steel Rods. Figures are based on [47]

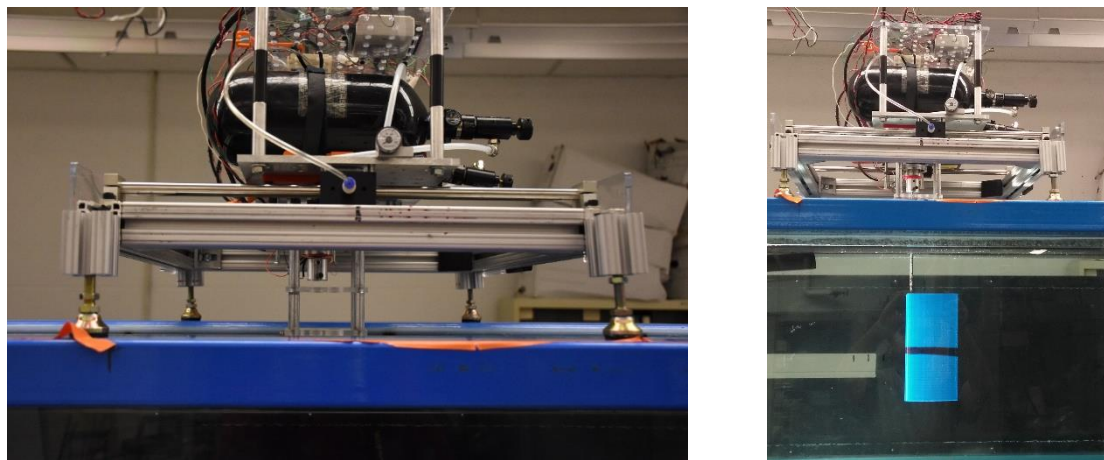


Figure 2.5: Experimental Rig

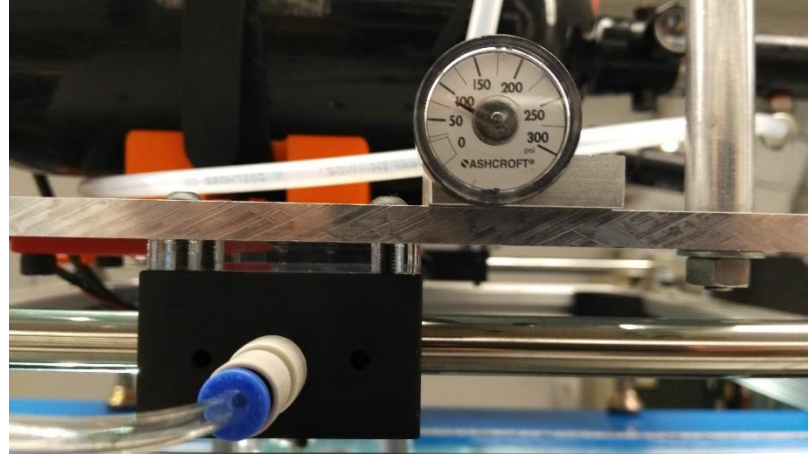


Figure 2.6: Air bearing floating on the steel rod and pressure gauge

A plastic extension is attached to the front of the two acrylic sheets (friction fit). It is made of two parts, one projecting four solid cylinders (referred to as Part B) and another projecting four hollow cylinders (referred to as Part A) into which the cylinders of the Part B are inserted (Figure 2.7). This allows free sliding motion along the axis of the cylinders, allowing for variation of length. Part B holds the stationary hydrofoil. There are rows of apertures in both the hollow and solid cylinders. Each aperture is at a distance of 1 cm from its preceding one. Aligning these apertures and locking them by passing screws through them allows for maintenance of a given length. The distance between the trailing edge of the first hydrofoil and the leading edge of the second is restricted between one and two chord lengths. This allows for direct comparison with similar works; also on going beyond these lengths, the effect of the stationary reduces significantly. Keeping the foils closer interferes the formation of the vortices behind the hydrofoil.



Figure 2.7: From left to right: 1) Part B holding the stationary hydrofoil 2) Part B inserted into Part A

The hydrofoils are NACA 0012, which are a good match for approximating the cross section of some of the larger fins in nature [16]. The foils have a chord length of 10 cm and a span length of 20 cm. The CAD model for the foils was created using coordinates imported from NASA's aerofoil database, and a spline curve was fit on the points in SOLIDWORKS (132 in total). Both rigid foils were printed using rapid prototyping (Printer model: Stratasys - Dimension SST 1200es™; Material: ABSplus). PIV videos are taken with the laser illuminating a sheet passing halfway along the length of the foil. The hydrofoils are always aligned in a straight line with their mean chords parallel to the direction of flow. The entire rig is positioned so that the hydrofoils always lie in the middle of the tank.

Care is taken to ensure that the rig on the air bearings is in its neutral position along the rod when the load cell is connected to it, to prevent skewing of results. The entire rig, while stationary, was allowed to float on the air bearings and given small disturbances to move it. Each time the place along the guideways at which it comes to rest was noted. The average of these points was calculated and the length of the attachment that connects the strain gauge to oscillating foil has been adjusted to the same. The rig has four independently adjustable legs to ensure that the rods are horizontal.

Finally, the entire setup is operated using LabVIEW. The program allows the user to set the frequency and amplitude of oscillation, as well as the neutral position of the oscillating hydrofoil. The domain of each of the parameters is given in Table 2.

<i>Parameter</i>	<i>Domain</i>	<i>Units</i>
<i>Frequency</i>	0.5, 0.75, ..., 1.75	Hz
<i>Amplitude</i>	10, 20, 30, 40	Half sweep angle in degrees
<i>Distance of separation</i>	20, 25, 30/2, 2.5, 3	Cm/C
<i>Flexibility of fin</i>	Rigid, Flexible	N/A

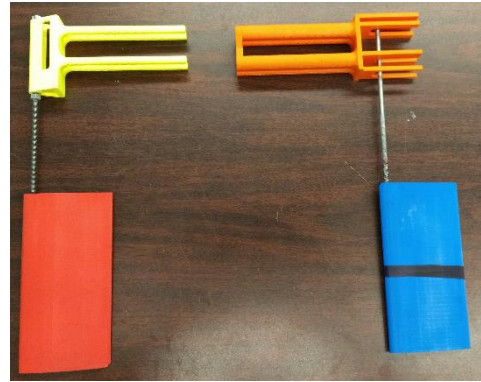
Table 2: Parameter Domains and Units

A small timer delay in the program allows the user to delay the beginning of oscillation of the hydrofoil.

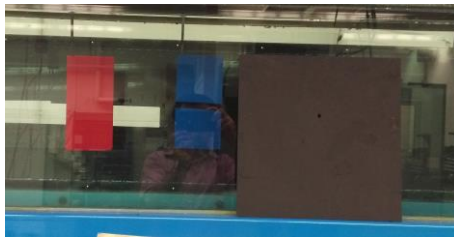
For the flexible hydrofoil experiments, the lagging rigid foil is replaced with a flexible one with identical dimensions. The leading hydrofoil is still rigid. The first 1/4th of the hydrofoil is printed using rapid prototyping, the rest is silicone, attached using the three anchors as shown. It is created using a mould of the NACA 0012 foil shape. The mould was printed using rapid prototyping. This ensures that the leading edge of the hydrofoil always undergoes sinusoidal pitching motion, and does not slip on the driving rod as the silicone would. Sinusoidal motion is a biologically accurate choice, proven in [66] [67] [68].



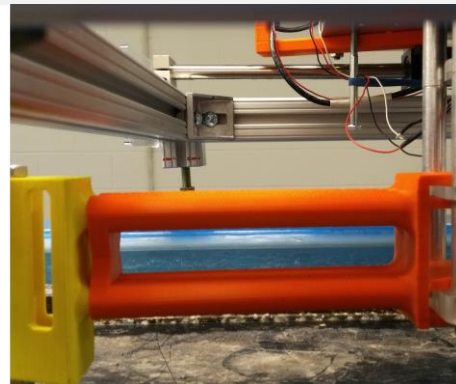
(a)



(b)



(c)



(d)

Figure 2.8: a) Flexible hydrofoil b) Double fin configuration schematic c) double fin configuration d) attachment of Parts A and B to experimental rig

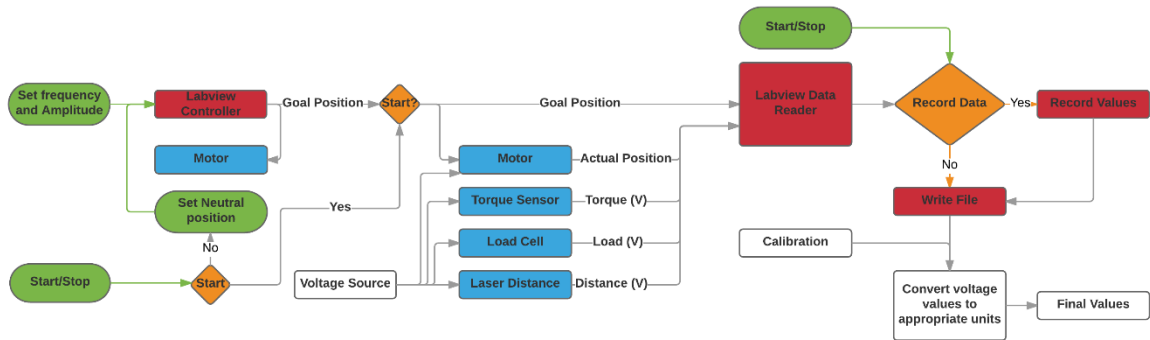


Figure 2.9: Schematic of Experimental Data Flow/Protocol

Colour	Implication
Green	User Input
Red	Via LabVIEW or LabVIEW operation
Blue	Sensor or actuator
Orange	Option

Table 3: Key for figure 2.7

Test protocol:

1. Perform calibration for the sensors
2. Attach the hydrofoil to the motor
3. If testing the double fin configuration, attach Part A and Part B with hydrofoil
4. If free swimming, remove the load cell and find the neutral position of experimental rig on air bearings
5. Set the hydrofoil initial position parallel to direction of flow
6. Switch on all the voltage supplies (to motor, torque sensor, laser distance sensor)
7. Start the pump
8. Set the frequency of oscillation, the amplitude of oscillation and the data file name in LabVIEW and start running the program
9. Open the valves to pressure the air bearings
10. Check for jumps in initial values to ensure that the voltage supply is connected
11. Check readings of actual position to ensure smooth motion of the hydrofoil
12. If free swimming, wait until the rig returns to and oscillates about the neutral position
13. Wait 15 seconds (minimum) then begin data recording
14. End data recording
15. Stop LabVIEW program, close the valves to depressurise the air bearings and stop the pump.

Test parameters:

1. Input/controlled parameters:

- a. Amplitude of oscillation (Degrees)
- b. Frequency of oscillation (Hz)
- c. Distance of separation (cm/C)
- d. Flow speed (in/s) (Input parameter for acceleration condition, controlled and recorded for free-swimming condition)

2. Output parameters:

- a. Instantaneous torque (V)
- b. Angular position of hydrofoil (Degrees)
- c. Distance of hydrofoil from end of experimental rig (if free swimming) (cm)
- d. Thrust (if in acceleration condition) (V)
- e. Time (ms)
- f. Flow speed (in/s) (Input parameter for acceleration condition, controlled and recorded for free-swimming condition)

Calculation of results from these outputs is discussed in the Section 2.3.

2.2 PIV Setup

As mentioned before, a secondary aim of this thesis is the development of an inexpensive and sufficiently robust PIV technique to quantify flow fields. The setup uses a DSLR camera and a continuous laser, compared to the high-speed cameras and pulsing lasers of commercially available PIV systems. [69] [70] [71] were referred to for background information.

During the validation tests described in Chapter 4, the camera is kept stationary and used to capture a video of the flow at various constant speeds. The frames are processed using MatPIV and the results have been compared to the flow speed measured using the anemometer.

Measurements of flow were obtained using a custom-built particle image velocimetry (PIV) experimental setup. A 500 mW diode-pumped solid-state laser (532nm DPSS Laser System; Laserglow Technologies® Hercules Series) was positioned centrally on a camera tripod and clamped; its beam directed horizontally into the side of the tank. The continuous wave laser produced a 532 nm wavelength green light, which was directed through a convex lens (Plano Concave Cylindrical Lens; Thor Labs®) to produce a 2-dimensional laser sheet measuring approximately 20 cm in width on average, with a thickness of 5 mm, through the breadth of the tank. The lens was held in a custom-made 3D printed part, mounted on the laser using 3 set screws. A black acrylic sheet was used for some tests to reduce the reflection of light from the glass at the further end of the water tunnel, and for reasons of safety. Parallelism was maintained using a spirit level at the laser as well as ensuring the weak reflected beam was at the same height as the laser as shown below in Figure 2.10.

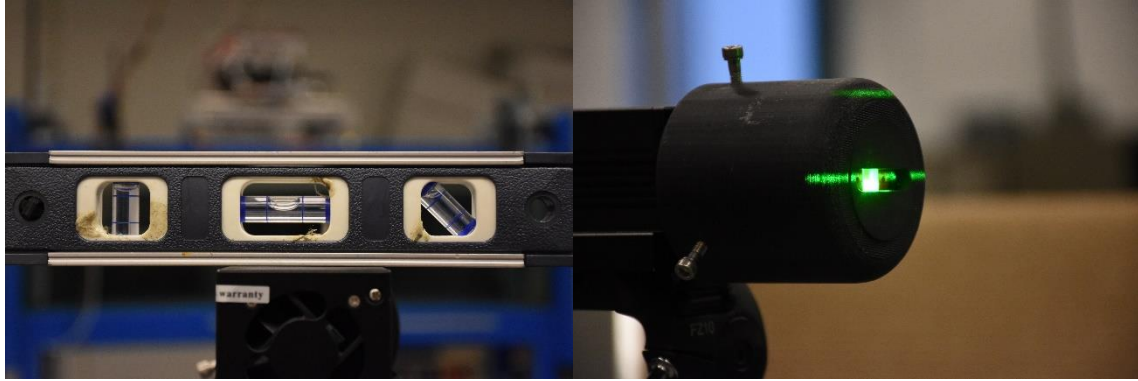


Figure 2.10: Ensuring a horizontal plane

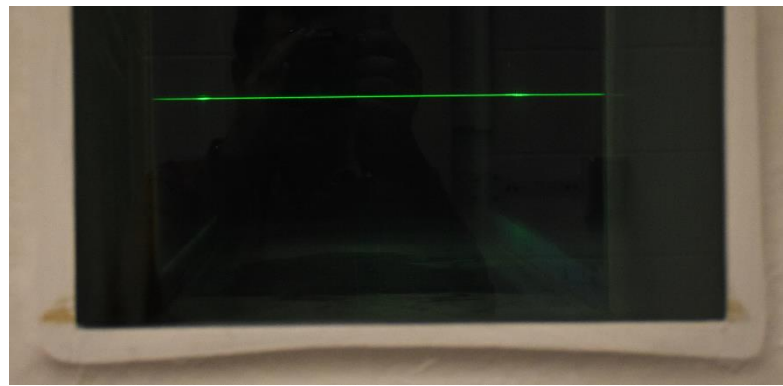


Figure 2.11: Resulting laser plane

Unlike a conventional commercial PIV system, which pulses the laser light and synchronizes the image capture, the laser in this system is constantly on and the image capture occurs continuously. Perpendicular to the laser sheet a digital single-lens reflex (DSLR) camera (D7200; Nikon Corporation®) with a macro lens (AF-S DX NIKKOR 18-140mm f/3.5-5.6G ED VR; Nikon Corporation®) was mounted on a tripod. Figure 2.12 illustrates the experimental PIV setup. The DSLR camera was set to record in video mode at full high definition resolution of 1920 x 1080 pixels at a frame rate of 60 frames per second (fps). The camera focus was manually set so as to focus on the particles illuminated by the laser sheet, and the shutter speed was set to $1/320$ s with an ISO of 2000 in order to minimize particle

streaking while increasing the sensitivity of the camera sensor to low light. The resulting noise was negligible; tests at ISOs of ~ 4000 also gave good results.

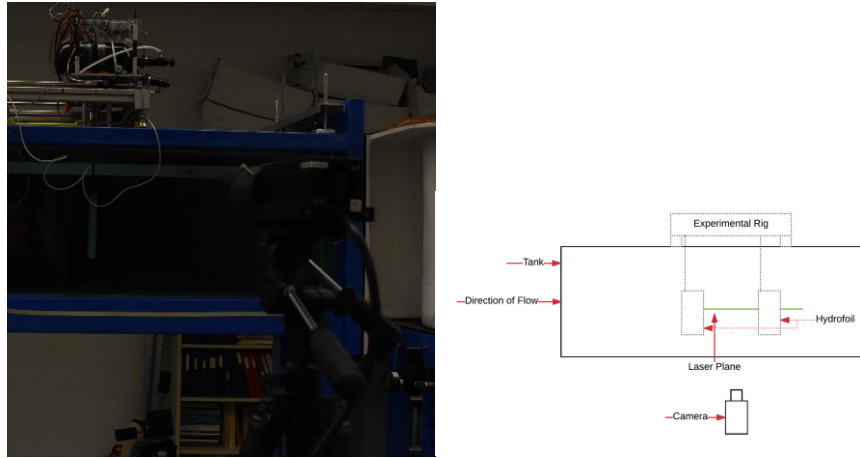


Figure 2.12: From left to right 1) PIV Setup 2) PIV Setup Schematic

The water tunnel was seeded with neutrally buoyant $11\text{ }\mu\text{m}$ silver-coated glass spheres (Potters Industries®) assumed to follow the fluid flow. Correct particle density ensured the absence of peak locking, while giving accurate information of the flow. It also ensured approximately 5-7 particles within the smallest interrogation window size.

Using the MATLAB Image Processing Toolbox, video records of raw PIV data were converted to a series of individual still frames. Paired images in sequence were used to cross-correlate particle matching required to estimate velocities. This was done using MatPIV version 1.6.1. ([60] [69]). This script uses a hybrid particle image velocimetry/particle tracking velocimetry approach creating an iterative displacement estimating function. Successive interrogation windows in a given iteration/pass over the entire image of fixed window size used a 50% overlap, and successive passes used windows of decreasing size. The window sizes implemented measured 256×256 , 128×128 , 64×64 and 32×32 .

Further analysis was run using the same interrogation window sizes, but twice using each of the above size, to ensure accuracy. For this window size and overlap, velocity estimates were produced at a final, physical resolution of approximately 0.41 cm x 0.41 cm. Spurious vectors were identified using global mean and local median filters (3 and 2.5 standard deviations, respectively), and outliers were replaced using a linear interpolation of neighbouring vectors.

2.3 Experimental Procedure and Data Analysis:

This section briefly describes experimental setup when performing different types of tests; specifically, it details the changes in the setup when conducting tests under acceleration and under free-swimming conditions.

2.3.1 The effect of amplitude and frequency of oscillation, distance of separation, and flexibility of the foil under free swimming conditions:

For free-swimming conditions, the load cell is not connected, and removed from the rig. After aligning the hydrofoils along the direction of the flow, the air bearings are pressurised. The frequency and amplitude of oscillation of the lagging hydrofoil are set. The flow speed is varied until the setup maintains the previously observed neutral position visually. While there is some oscillation, the average position remains within ± 1.5 cm from the neutral position. This leads to an error of ± 0.254 cm per second in calculating the free-swimming speed. The position is rechecked by checking the corresponding the laser distance readings. The data collection is then begun.

2.3.2 The effect of amplitude and frequency of oscillation of the foil under acceleration:

In this setup, the load cell is connected to the experimental rig and the rod of the oscillating hydrofoil, constraining the movement of the hydrofoil. The speed of flow and the frequency and amplitude of oscillation of the lagging hydrofoil are set and the air bearings are pressurised. Data collection is started 15 seconds after the anemometer shows that the set flow speed has been achieved.

It is ensured during analysis that the position and direction of motion of the foil at the start and end point of the data under consideration is the same to prevent skewing of data. The

data contains at least 10 ten periodic oscillations of the hydrofoil, with up to forty for high frequencies.

2.3.3 Data analysis

The load cell was calibrated daily ensuring that the calibration is correct for every set of experiments. Torque was calibrated before every set of experiments. The data from the load cell and the torque sensor is recorded in terms of raw voltages by the LabVIEW program, along with time, laser distance sensor readings, goal position at the given time instant, and actual position at the given time instant. It is then converted to appropriate units using the aforementioned calibration. The angular velocity is calculated in radians based on the actual position of the motor at a given time instant. The readings are recorded at a rate of approximately 28 Hz.

Net thrust is calculated by averaging the force recorded by the load cell over time. It is expected that near the end points of the amplitude, the net force will be negative as the drag is greater than the thrust generated.

The work done is calculated using the product of the instantaneous torque and the instantaneous angular velocity. Since these are sinusoidal curves out of phase, there exist both positive and negative values. To ensure accuracy, the average value of torque is confirmed to be $O(-15)$ Nm. While the formula for the exact calculation of work done would be $\int_{t_1}^{t_2} T(t) \cdot \omega(t) \cdot dt$, it is discretised into $\sum_{t_1}^{t_2} T(t) \cdot \omega(t)$, where t_1 and t_2 are the start and end time respectively of the subset of data collected under consideration, whose difference in values is an integral multiple of the time period of oscillation of the hydrofoil.

This is the mechanical work done and differs from input power in terms of electrical energy as the power consumed is always greater than zero, while work done here has negative values when the torque is applied in the direction opposite to the direction of motion.

To reiterate, efficiency (η) is calculated as the ratio of thrust produced to work done and economy(η') is calculated as the ratio of free-swimming speed to work done. The work done and thrust produced are both averaged over the repeated tests using the same input parameters.

Strouhal number (St) is defined as the ratio of the product of frequency (f) and pitch amplitude (A') to the speed of incoming flow (s).

$$\eta = \frac{\textit{Average thrust}}{\textit{Average work done}}$$

$$\eta' = \frac{\textit{Free - swimming speed}}{\textit{Average work done}}$$

$$St = f * A' / s$$

Chapter 3: Results

This study consists of four experimental sets. In each set of experiments the main comparison is always between the single and double hydrofoil configuration (Fig. 2.3).

1. Effect of amplitude and frequency during acceleration on thrust, work done and efficiency
2. Effect of distance of separation between hydrofoils during acceleration on work done
3. Effect of distance of separation between hydrofoils and frequency of oscillation during free swimming on swimming speed, work done and economy
4. Effect of flexibility of oscillating hydrofoil on free swimming speed, work done and economy

Table 5 lists the range of values under consideration for each experimental set.

<i>Experiment set</i>	<i>Frequency (f) (Hz)</i>	<i>Amplitude (A) (Half sweep in degrees)</i>	<i>Swimming speed (s) (cm/s)</i>	<i>Distance of separation (cm)</i>
1.	{0.5, 0.75, ..., 1.75}	{10, 20, 30, 40}	{7.62, 10.16}	20
2.	{0.5, 0.75, ..., 1.5}	20	{7.62, 10.16}	20, 25, 30
3.	{0.5, 0.75, ..., 1.5}	20	Free swimming	20, 25, 30
4.	{0.5, 0.75, ..., 1.5}	20	Free swimming	20, 25, 30

Table 4: Range of parameter values for experiment sets

<i>Experiment Set</i>	<i>Repetitions of test (r) (minimum)</i>	<i>Repetitions of test (average)</i>	<i>Parameter Space (#(A x f x s x r x d))</i>
1.	3	4	144
2.	3	4	108
3.	3	5	54
4.	3	4	54

Table 5: Parameter Space for Experimental Sets and Repetitions

Format of the results:

The graphs for the double hydrofoil configuration shown in this chapter are normalised using the corresponding values of the single hydrofoil configuration to allow for direct comparison. Hence the value of A (thrust, free swimming speed, work done, or efficiency) for the double hydrofoil configuration at frequency X (e.g. 1 Hz) and amplitude Y (e.g. 20 degrees) is normalised using the corresponding value of A for the single hydrofoil configuration at the same frequency X (1 Hz) and amplitude Y (20 degrees). Hence the normalisation value for each point in graph is different, leading to a different percentage error. Error margins are discussed in greater detail in section 3.5. This also allows direct comparison between double and single hydrofoil configurations.

Care is taken to ensure that averages are calculated over a time period with an integral number of oscillations to prevent skewing. A minimum of ten time periods is considered, with a maximum of forty.

Note that via this normalization:

1. A ratio <1 for speeds/thrust implies the double fin configuration moves at lower speeds/generates less net thrust at the selected frequency and amplitude as compared to the single foil configuration
2. A ratio <1 for work done implies that the double fin configuration requires less energy to move at the selected frequency and amplitude as compared to the single foil configuration
3. A ratio <1 for efficiency/economy implies that the double fin configuration is less efficient/economical at the selected frequency and amplitude as compared to the single foil configuration

3.1 Experiment Set 1 - Effect of amplitude and frequency during acceleration on thrust, work done and efficiency

The first set of experiments examines the influence of the stationary foil on performance during acceleration. The thrust produced, work done and efficiency are calculated. Efficiency is defined as the ratio of thrust produced to work done. While the work done for the double hydrofoil configuration is less than the work done by the single hydrofoil configuration, the double hydrofoil configuration also produces less thrust than the single hydrofoil configuration. Efficiency increases with frequency, but the single hydrofoil configuration is consistently better than the double hydrofoil configuration.

Figure 3.1 clearly shows that the ratio of thrust generated increases with increasing frequency and amplitude. The figure also shows that for the higher amplitudes and frequencies, the ratio of thrust produced moves close to 1, implying that the thrust produced by both the single and double hydrofoil configuration is almost equal.

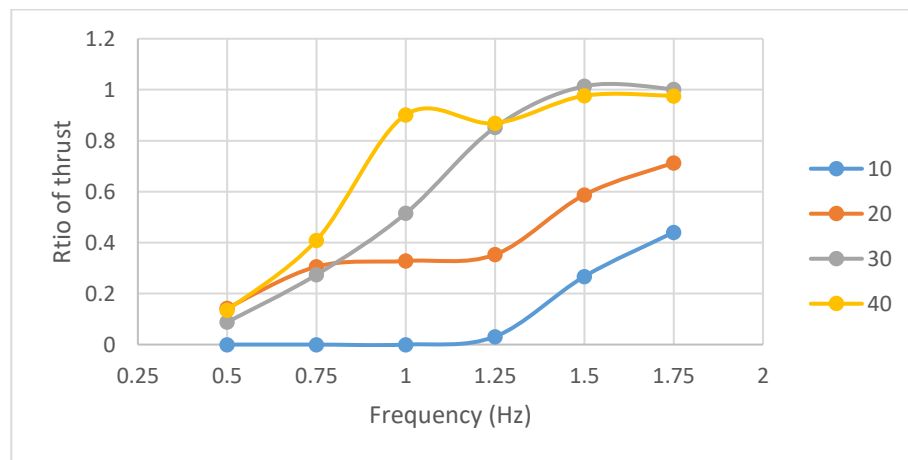


Figure 3.1: Ratio of thrust produced for double hydrofoil to single hydrofoil configuration at a given amplitude v/s frequency when the speed of oncoming flow is 7.62 cm/s. Each curve represents a given amplitude of oscillation, whose half sweep values are noted as legends.

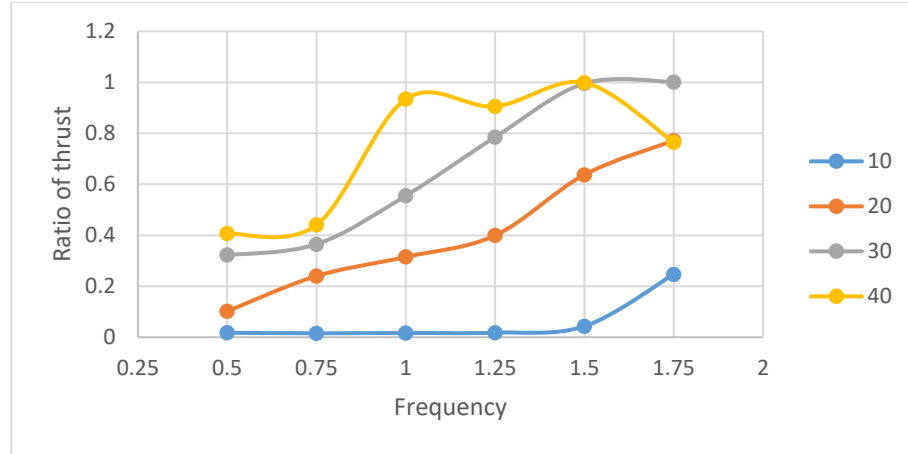


Figure 3.2: Ratio of thrust produced for double hydrofoil to single hydrofoil configuration at a given amplitude v/s frequency when the speed of oncoming flow is 10.16 cm/s. Each curve represents a given amplitude of oscillation, whose half sweep values are noted as the legends.

The drag on the stationary leading hydrofoil is an additional source of drag for the double hydrofoil configuration as compared to the single hydrofoil configuration. Since:

1. the thrust generated by the pitching hydrofoil is small at lower amplitudes and frequencies
2. the thrust generated by the pitching hydrofoil increases significantly with increasing frequency and amplitude
3. the magnitude of drag on the stationary hydrofoil only slightly increases with increasing flow speed

the drag on the stationary hydrofoil has a more prominent effect on net thrust at lower frequencies and amplitudes.

The errant point of 40 degrees amplitude and 1.75 Hz frequency of oscillation is caused by the restriction on the maximum achievable torque of the motor. Under these conditions the motor is unable to generate the required torque causing an erratic motion pattern.

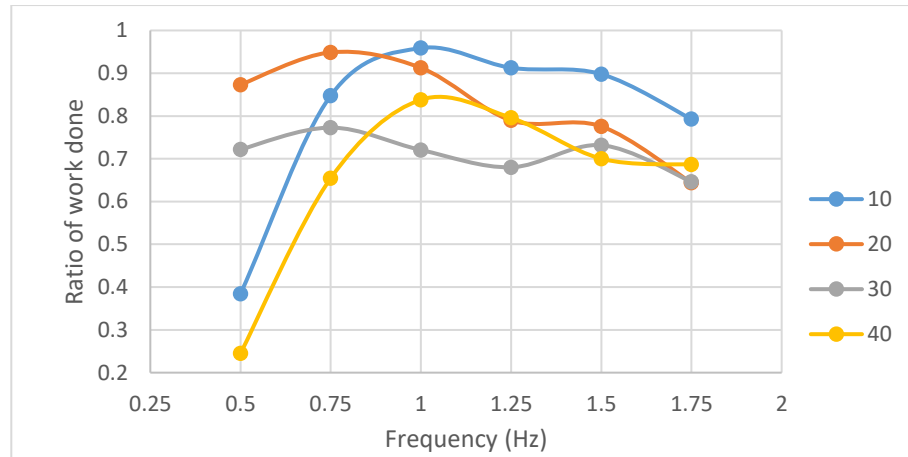


Figure 3.3: Ratio of work done for double hydrofoil to single hydrofoil configuration at a given amplitude v/s frequency when the speed of oncoming flow is 7.62 cm/s. Each curve represents a given amplitude of oscillation, whose half sweep values are noted as the legends.

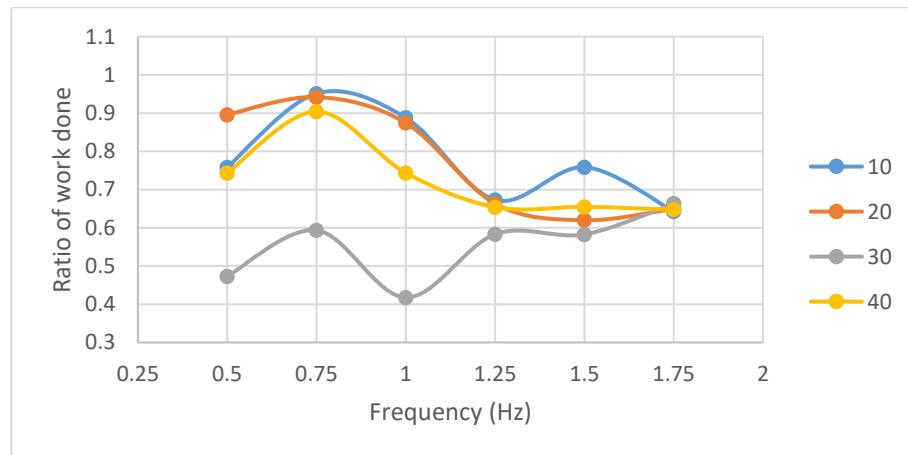


Figure 3.4: Ratio of work done for double hydrofoil to single hydrofoil configuration at a given amplitude v/s frequency when the speed of oncoming flow is 10.16 cm/s. Each curve represents a given amplitude of oscillation, whose half sweep values are noted as the legends.

The ratio of work done stays around 0.7 ± 0.2 . This shows that the work done is, on average, 30% less in the double hydrofoil configuration as compared to the single hydrofoil configuration.

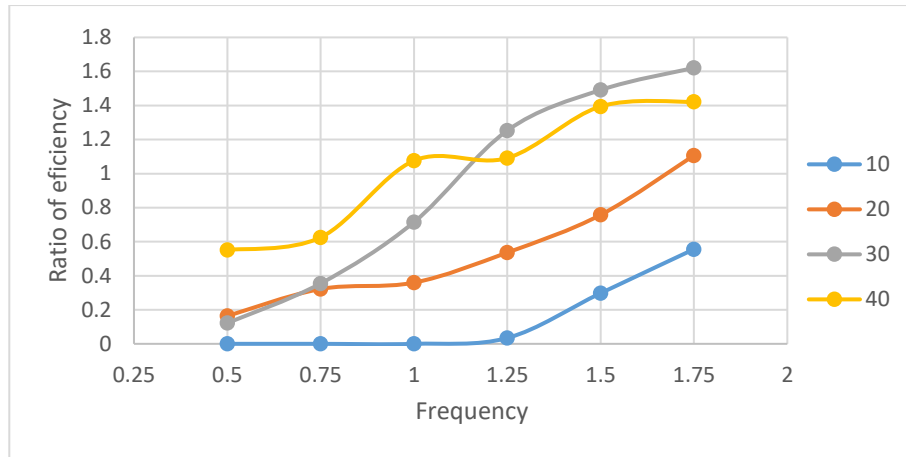


Figure 3.5: Ratio of efficiency for double hydrofoil to single hydrofoil configuration at a given amplitude v/s frequency when the speed of oncoming flow is 7.62 cm/s. Each curve represents a given amplitude whose values are noted as legends.

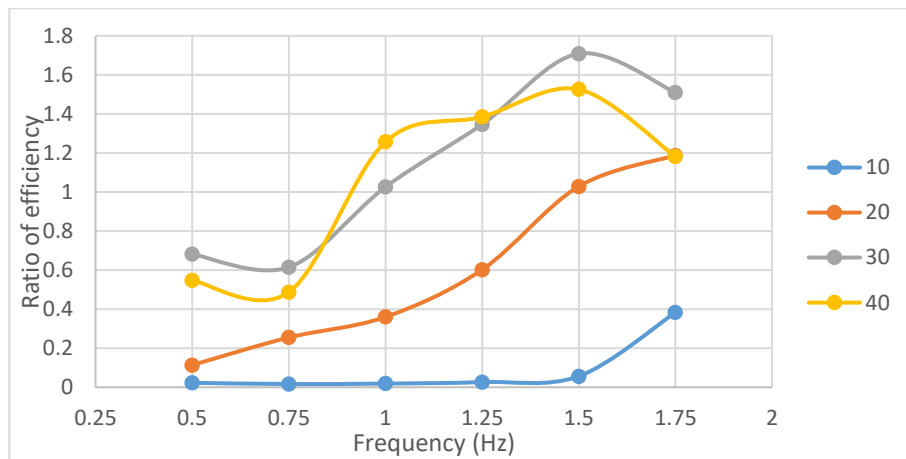


Figure 3.6: Ratio of efficiency for double hydrofoil to single hydrofoil configuration at a given amplitude v/s frequency when the speed of oncoming flow is 10.16 cm/s. Each curve represents a given amplitude whose values are noted as legends.

As seen from Figures 3.5 and 3.6, the ratio of efficiency for higher frequencies and amplitudes crosses 1, implying that under these conditions the double hydrofoil configuration is better than the single hydrofoil configuration.

3.2 Experiment Set 2 - Effect of distance between hydrofoils during acceleration on work done

This set of experiments examines the influence of distance of separation between the stationary hydrofoil and the pitching hydrofoil on performance during acceleration. Amplitude is kept constant while frequency and distance of separation between the hydrofoils are varied. The work done is calculated.

While the work done for the double hydrofoil configuration is less than the work done by the single hydrofoil configuration, this difference reduces as the distance of separation between the hydrofoils is increased. At large distances of separation, the work done by the double hydrofoil configuration almost equals the work done by the single hydrofoil. The distances chosen represents 2, 2.5 and 3 chord lengths of the hydrofoil.

Figures 3.9 and 3.10 shown below plotted with each curve representing a constant distance of separation show that for a given frequency the ratio of work done always increases with increasing distance of separation while accelerating.

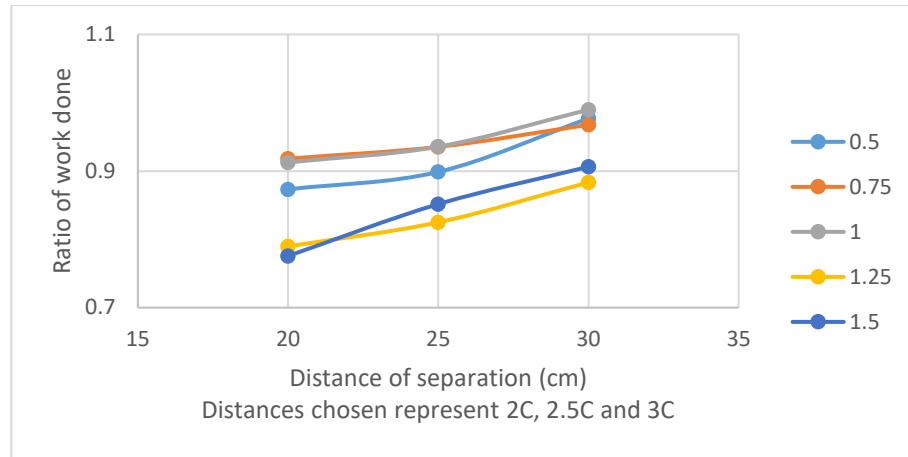


Figure 3.7: Ratio of work done for double hydrofoil configuration to single hydrofoil configuration at a given speed (7.62 cm/s), amplitude (20 degrees) and frequency of oscillation v/s distance of separation. Each curve represents a given frequency of oscillation whose values are denoted as legends.

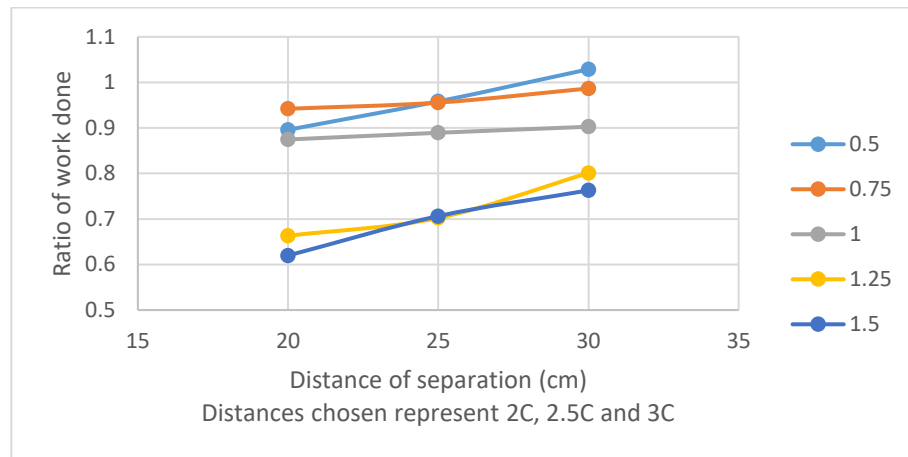


Figure 3.8: Ratio of work done for double hydrofoil configuration to single hydrofoil configuration at a given speed (10.16 cm/s), amplitude (20 degrees) and frequency of oscillation v/s distance of separation. Each curve represents a given frequency of oscillation whose values are denoted as legends.

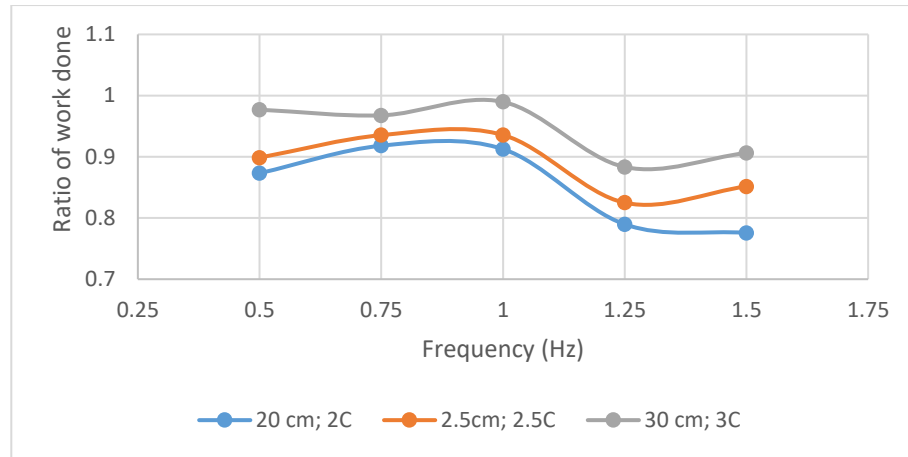


Figure 3.9: Ratio of work done for double hydrofoil to single hydrofoil configuration at a given amplitude (20 degrees) v/s frequency when the speed of oncoming flow is 7.62 cm/s. Each curve represents a given distance of separation whose values are noted as legends.

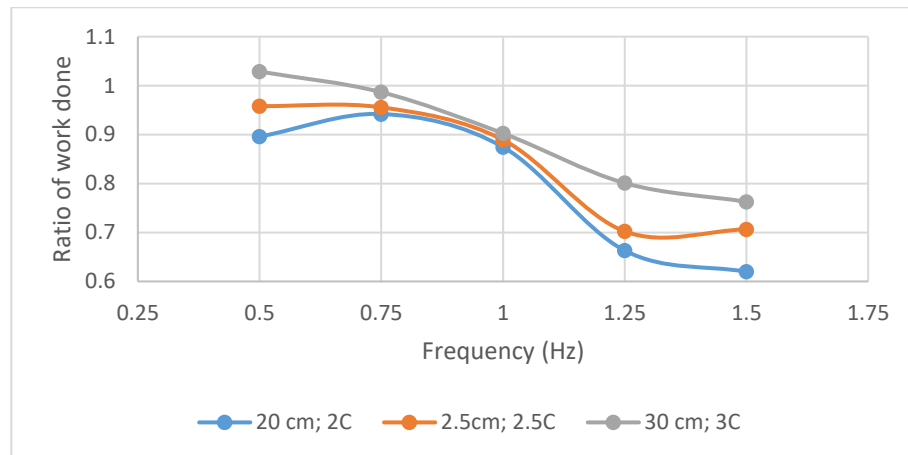


Figure 3.10: : Ratio of work done for double hydrofoil to single hydrofoil configuration at a given amplitude (20 degrees) v/s frequency when the speed of oncoming flow is 10.16 cm/s. Each curve represents a given distance of separation whose values are noted as legends.

3.3 Experiment Set 3 - Effect of distance between hydrofoils and frequency of oscillation during free swimming on swimming speed, work done and economy

This set of experiments focuses on studying the effect of distance of separation between the hydrofoils on free swimming speed, work done and economy. The economy is defined as the ratio of free-swimming speed to the work done by the hydrofoil. Note that the previous tests used efficiency as a measure of comparison. In these tests, the amplitude of oscillation is kept constant while the distance of separation between the hydrofoils is varied. Here the free-swimming speeds range from 10.69 cm/s to 31.75 cm/s and Strouhal numbers range from 0.3 to 0.4. Figures 3.11-3.13 present the normalized speed, work done, and economy for these tests.

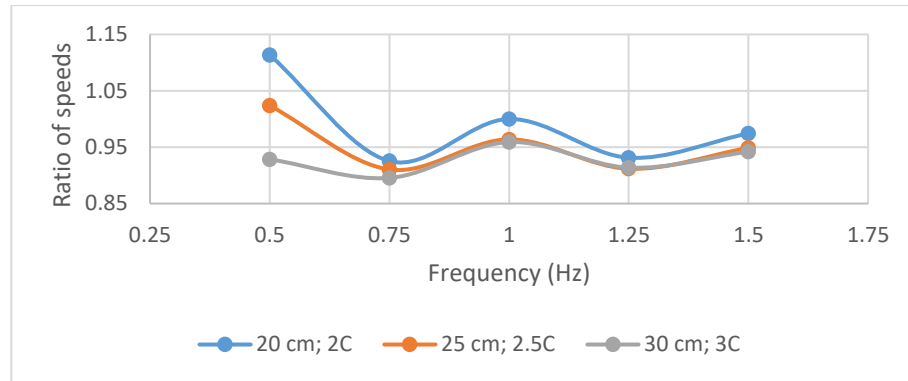


Figure 3.11: Ratio of speeds of double hydrofoil to single hydrofoil configuration at a given amplitude (20 degrees) v/s frequency under free swimming conditions. Each curve represents a given distance of separation whose values are noted as legends.

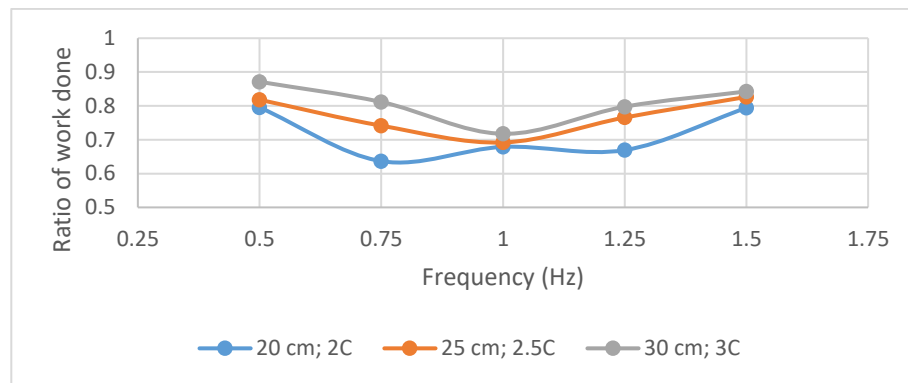


Figure 3.12: Ratio of work done of double hydrofoil to single hydrofoil configuration at a given amplitude (20 degrees) v/s frequency under free swimming conditions. Each curve represents a given distance of separation whose values are noted as legends.

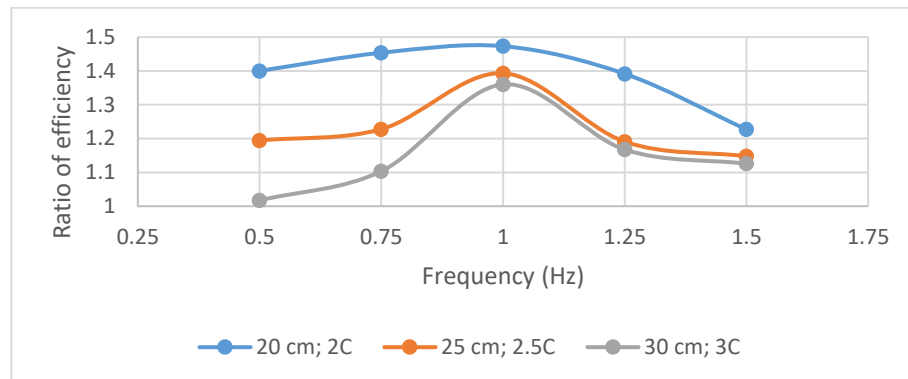


Figure 3.13: Ratio of economy for double hydrofoil to single hydrofoil configuration at a given amplitude (20 degrees) v/s frequency under free swimming conditions. Each curve represents a given distance of separation whose values are noted as legends.

As the results show:

1. The presence of the stationary hydrofoil reduces the speed of the double fin configuration as compared to that of the single fin configuration. This is expected as the addition of another hydrofoil, however hydrodynamic increases the drag on the entire configuration.
2. The stationary hydrofoil has a positive influence on the work done at all distances of separation. The work done to move the pitching hydrofoil reduces by $\sim 20\%$ in the presence of a stationary leading hydrofoil.
3. As the distance of separation increases the effect on work done reduces. Among the tests conducted here, a distance of separation of 20 cm, i.e. 2 chord lengths (C) minimises work done and thus maximises economy.
4. The results also show that at 1 Hz the system shows the maximum reduction in work done as well as a smaller than expected reduction in free-swimming speed. Due to this the economy at 1 Hz is the greatest as compared to other frequencies at a given distance of separation. As no changes were made in the experimental setup for this entire experimental set, it is possible that there exists a resonance in the system at this frequency.

Here the ratio of work done is consistently below 0.9 in the tested range; the values for the ratio of speeds are also below 1 but stay around 0.9, while the ratio of work done drops to 0.7.

This ensures that the economy is consistently above 1 for the tested range. It must be noted that with increasing the distance of separation, the work done increases.

The reduction in work done is of particular interest as it shows that at free swimming, the presence of a stationary hydrofoil at the given distances actually increases the overall economy, in addition to its function of providing stability.

As discussed in section 3.1, the effect of drag on the stationary hydrofoil on net thrust reduces with increasing frequency and speed of flow.

3.4 Experiment Set 4 - Effect of flexibility of oscillating hydrofoil on free swimming speed, work done and economy

This set of experiments focuses on the effect of flexibility of the hydrofoil. Experiments similar to those run in the previous set are run, the only difference being that the rigid pitching hydrofoil is replaced by a flexible hydrofoil made from silicone as described in Chapter 2. Also, the values of free swimming speed, work done and economy are compared to those of a single flexible hydrofoil. These are also the values used for normalization.

Here the free-swimming speeds range from 9.14 cm/s to 24.38 cm/s and Strouhal numbers range from 0.38 to 0.45.

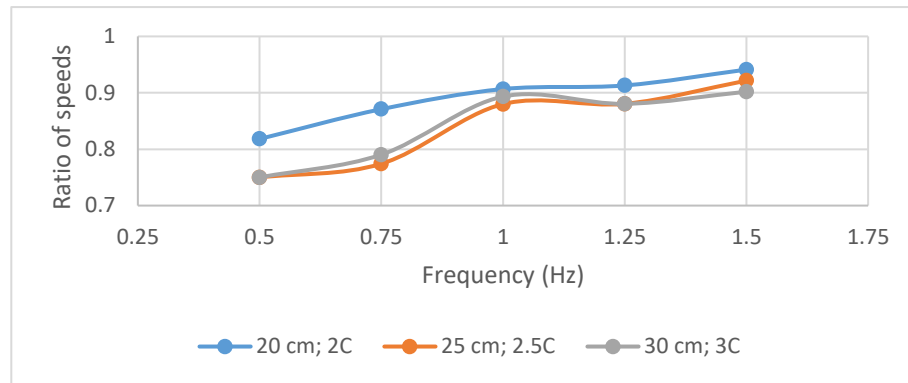


Figure 3.14: Ratio of speeds of double hydrofoil to single hydrofoil (flexible) configuration at given amplitude (20 degrees) v/s frequency. Each curve represents a given distance of separation whose values are noted as legends.

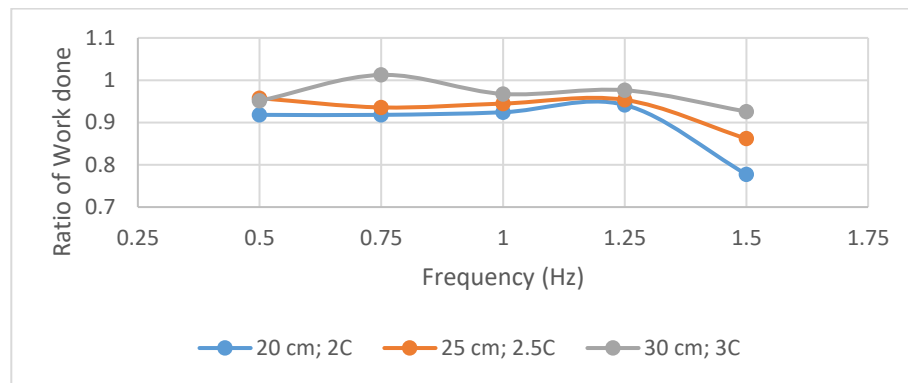


Figure 3.15: Ratio of work done of double hydrofoil to single hydrofoil (flexible) configuration at given amplitude (20 degrees) v/s frequency. Each curve represents a given distance of separation whose values are noted as legends.

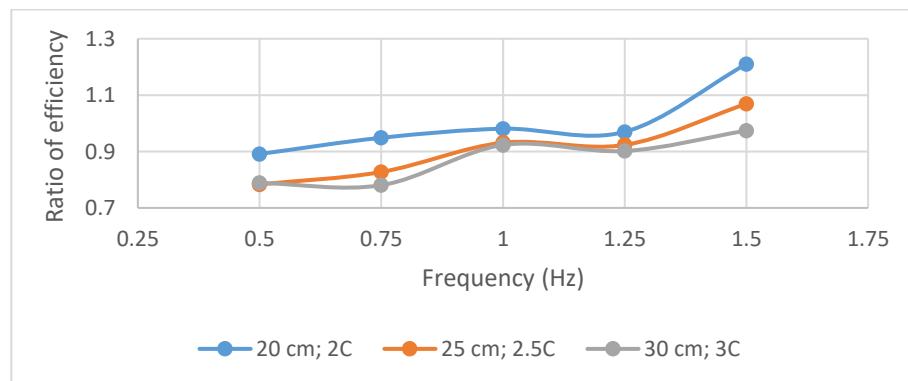


Figure 3.16: Ratio of efficiencies of double hydrofoil to single hydrofoil (flexible) configuration at given amplitude (20 degrees) v/s frequency. Each curve represents a given distance of separation whose values are noted as legends.

As the results show:

1. The presence of the stationary hydrofoil reduces the speed of the flexible double hydrofoil configuration as compared to that of the single hydrofoil configuration. While the higher frequencies show ratio values between 0.9 and 1, the others are significantly lower. This is expected as magnitude of thrust generated by the flexible hydrofoil is not very high.
2. The stationary hydrofoil has a positive influence on the work done at all distances of separation. The ratio of work done is consistently below 1 for all the test cases showing that even for the flexible foil configuration, the presence of a stationary leading hydrofoil reduces the work done to move the pitching hydrofoil.
3. In the case of the flexible double fin configuration the effect of the stationary hydrofoil on thrust is greater than its effect on the work done. This causes the economy for the flexible double fin configuration to be lower than that of a flexible single fin configuration for most of the values in the parameter space of this experiment set.
4. As the distance of separation increases the effect on work done reduces. This suggests the existence of an optimal distance of separation. Within the chosen parameter space, 1.5 Hz appears to be the optimal frequency for maximum economy. However, since the ratio of economy shows a rising trend, it is possible that higher frequencies would show a better ratio of economy.

The flexible double hydrofoil configuration does not perform as well as the rigid double hydrofoil configuration in terms of normalised values.

The drag on the leading hydrofoil has a greater effect on the flexible double hydrofoil configuration compared to the rigid double hydrofoil configuration as seen from their free-swimming speeds.

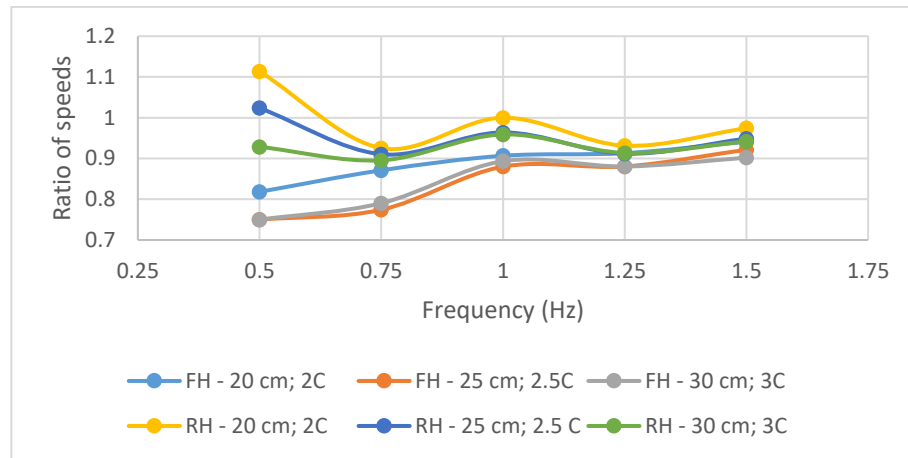


Figure 3.17: Ratio of free-swimming speeds for both rigid and flexible double fin configurations to their corresponding single fin configurations at a given amplitude (20 degrees) v/s frequency. Each curve represents a given type of hydrofoil and a given distance of separation whose values are noted as legends (RH – Rigid hydrofoil, FH – Flexible Hydrofoil).

The work done to move a rigid hydrofoil is significantly greater than the work done to move a flexible hydrofoil of similar dimensions. The effect of the presence of the stationary hydrofoil is also greater for the rigid hydrofoil as seen in Figure 3.18: Ratio of work done for both rigid and flexible double fin configurations to their corresponding single fin configurations at a given amplitude (20 degrees) v/s frequency. Each curve represents a given type of hydrofoil and a given distance of separation whose values are noted as legends (RH – Rigid hydrofoil, FH – Flexible Hydrofoil).Figure 3.18.

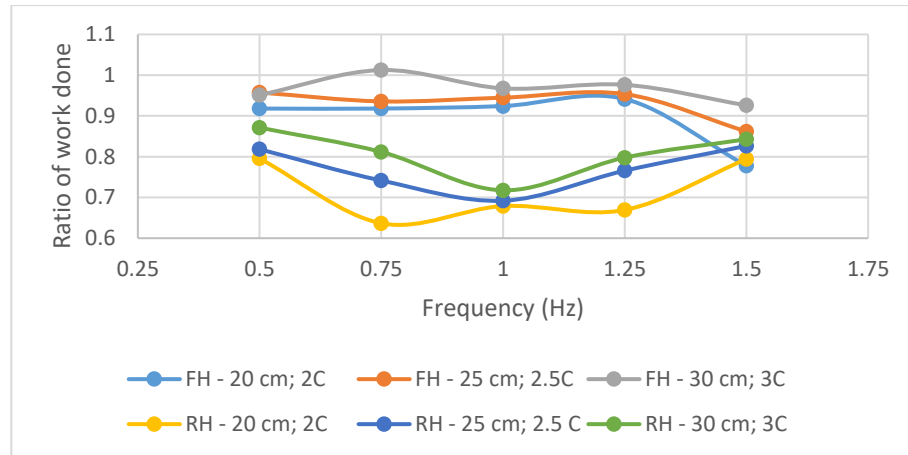


Figure 3.18: Ratio of work done for both rigid and flexible double fin configurations to their corresponding single fin configurations at a given amplitude (20 degrees) v/s frequency. Each curve represents a given type of hydrofoil and a given distance of separation whose values are noted as legends (RH – Rigid hydrofoil, FH – Flexible Hydrofoil).

Hence, while the flexible hydrofoils do significantly less work at given amplitude and frequency as compared to rigid hydrofoils, they also have lower free swimming speeds and produce less thrust. This leads to a smaller ratio of economy as compared to the rigid double hydrofoil configuration **Error! Reference source not found..**

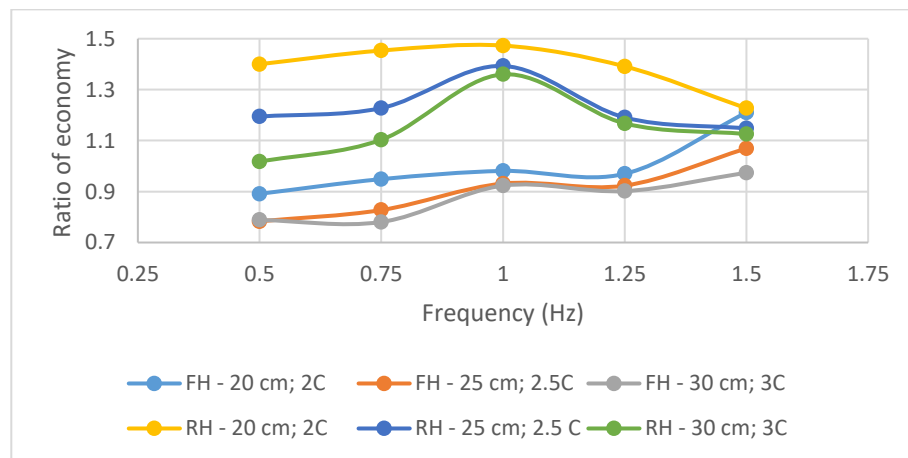


Figure 3.19: Ratio of economy for both rigid and flexible double fin configurations to their corresponding single fin configurations at a given amplitude (20 degrees) v/s frequency. Each curve represents a given type of hydrofoil and a given distance of separation whose values are noted as legends (RH – Rigid hydrofoil, FH – Flexible Hydrofoil).

This allows the rigid double hydrofoil configuration with a small distance of separation ($O(\sim 2C)$) have a better value of economy than the flexible single hydrofoil configuration.

3.5 Error analysis

Most of the experiments were performed while the scaling factor was the same down to the third decimal, hence ensuring that while taking the ratio of any of the parameters under consideration, any error in calculating the scaling factor would be cancelled out.

Error bars for thrust and torque are not shown on the graph as the errors are on the order of $O(4)$. This is due to the fact that the torque sensor used has an accuracy of $\pm 0.2\%$ and the load cell of $\pm 0.03\%$. The voltage values are directly read by the LabVIEW program. The error in calibration is independent on the weights ($O(2)$ g), but any such effect of scaling is negated by taking the ratio of double hydrofoil to single hydrofoil configuration.

Error in calculating ω , the instantaneous angular velocity of the hydrofoil is one possible source of error, as the recorded value is always an integer. Note that the error is largest at the end points of oscillation when the hydrofoil is at its slowest, and omega values are $1/30^{\text{th}}$ of their maximum value at the lowest amplitude and frequency of oscillation (i.e. lowest ω). Its effect is diminished with increasing amplitude. The maximum possible error is ± 0.5 degrees/s, which translates to ± 0.0087 radians/second. This value does however lead to ω being zero when it is not, with ω values being greater for the preceding and the next reading for ω . Since the torque is generally a continuous curve, this leads to a small overall error.

Error in finding free swimming speed is a relatively large source of error. While care has been taken to check that the average position of the hydrofoil over time is close to the neutral position, the fins at higher amplitude and frequency have larger oscillations along the direction of motion. This may be due to fluctuations in speed of flow as well. This has led to a ± 0.1 inches/second error in the lower free swimming speeds and ± 0.2 inches/second in the higher

free swimming speeds based on repeatability. The average of 3 tests was taken to reduce the effect of this error, increased to a sample size of 5 for higher speeds and amplitudes.

The error introduced by tilting of the stationary hydrofoil is considered. While the tilt caused the lowermost point of the hydrofoil to move towards the oscillating hydrofoil by a maximum of 1.5 cm, the midsection of the hydrofoil only moved back by 0.8 cm which is significantly less than the 10 cm chord length and 10 cm minimum distance between hydrofoils.

Finally, the error introduced by the bending of the oscillating hydrofoil rod is considered. The maximum bending is less than 0.6 inches in either direction at the bottom of the fin. This leads to an error of less than 3.6 cm overall. Since this is at the bottom of the fin, the errors effect is mitigated.

The following figures show the worst-case errors possible for free swimming speeds:

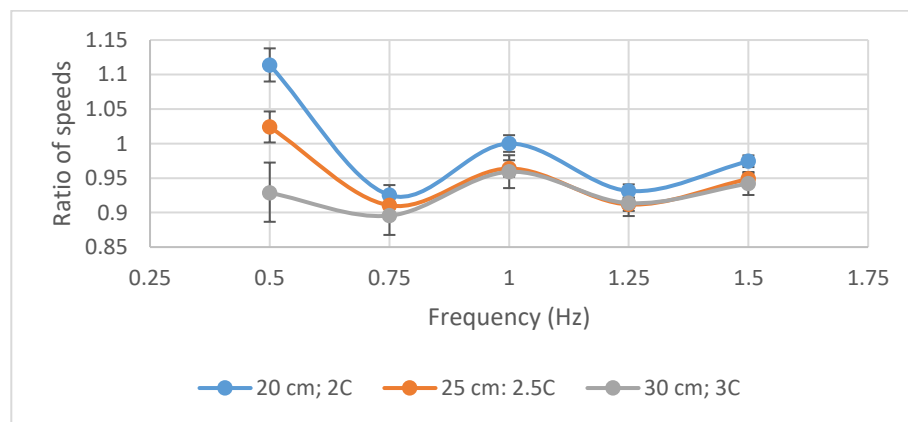


Figure 3.20: Ratio of speeds of double hydrofoil to single hydrofoil configuration at a given amplitude (20 degrees) v/s frequency under free swimming conditions. Each curve represents a given distance of separation whose values are noted as legends.

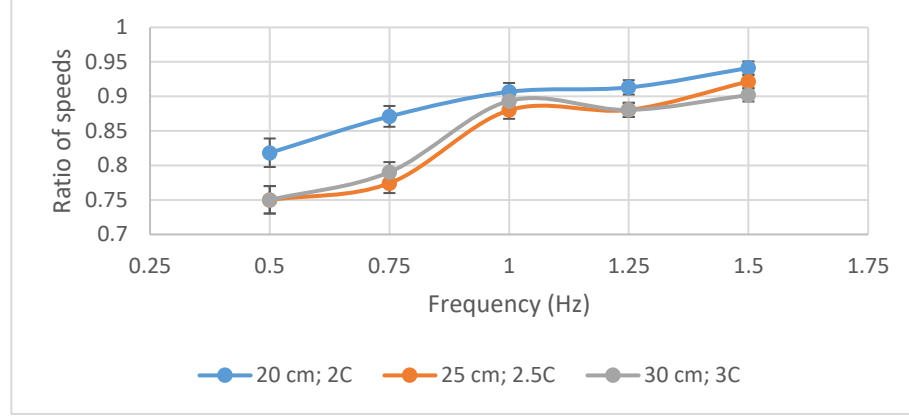


Figure 3.21: Ratio of speeds of (flexible) double hydrofoil to single hydrofoil configuration at a given amplitude (20 degrees) v/s frequency under free swimming conditions. Each curve represents a given distance of separation whose values are noted as legends.

The error in testing for free swimming speeds was ± 0.254 cm/s for low speeds and ± 0.508 cm/s for higher speeds. The standard deviation of the ratio of free swimming speed ranged from 0.015 at lower speeds (and frequencies) to 0.0105 at the highest speeds (and frequencies).

Standard deviation is calculated using the standard formula:

$$s_x = \sqrt{\frac{\sum_{i=1}^n (x_i - \bar{x})^2}{n - 1}}$$

The variation and errors in calculating the free-swimming speeds of the flexible hydrofoil are lower than those for the rigid hydrofoil for both single and double hydrofoil configurations.

Chapter 4: PIV Setup Validation and Analysis

As mentioned, the secondary aim of this thesis is the development of an inexpensive PIV system to quantify flow fields. The validation tests run for this setup as well as its limitations are discussed here.

4.1 Validation

While this setup has been used before, the improvements in camera technology constantly increase its use. This is the first time such a PIV setup has been used at a frame rate of 60 frames/second. As indicated in the literature review the code to run the analysis has been validated; it is the setup that requires the validation. Hence simple validation tests have been run to show its accuracy. Flows speeds from 2 to 10 inches/second have been selected, and the results in terms of average velocity (over 30 seconds) and error have been tabulated below.

SPEEDS (INCHES/S)	ANEMOMETER READING (INCHES/S)	AVERAGE PIV VALUE (INCHES/S)
2.5	2.6	2.4
5	5	5.1
7.5	7.4	7.3
10	9.9	10.2
UNCERTAINTY	± 0.05	± 0.05

As can be seen the setup is accurate to $\pm 4\%$. The accuracy of the setup in flows with vorticity is also tested. The flow behind a NACA 0012 foil is one of the most commonly simulated test cases.

A rectangular imaging area of greater length 30 cm was considered. The images taken captured a plane at mid-height along a 20 cm long hydrofoil. The speed of flow was 12.7 cm/s. The maximum previously seen is 6 cm/s. While it is possible to directly scale the results into the required units, to ensure simplicity and allow for direct comparison beyond the current size of imaging area, the results are presented with pixels as units. The flowing figures show the results of the tests.

The particles in this case are 4 pixels x 4 pixels on average. While the largest particles might be larger than 25 pixel² in the initial raw images, certain image processing algorithms are used to remove the edges with points of that are extremely low intensity. These points tend to vary as the particle moves along the laser sheet, and given their small magnitude, are also affected by reflections from other particles and changes in ISO settings of the camera. These algorithms however do not operate on pixels which contain values above a certain threshold.

Some particles might be 25 pixel² particle, larger than the 16 pixel² particles used in PIV experiments. However, the 16 pixel² particle size is recommended when the smallest interrogation window size is 16 pixels x 16 pixels, while in the tests presented here, smallest interrogation window size is 32 pixels x 32 pixels. While larger particles might increase computation time, they will also tend to increase accuracy.

The particle movement is restricted to under 2/3rd the minimum interrogation window size, which is larger than the ideal. Two reasons reduce the effect of this:

1. The interrogation windows are higher initially and progressively reduce in size

2. The windows progressively under consideration for a given window size can overlap by a user defined amount, allowing for a more accurate result

The main error here comes from the maximum speed of resolution. As we are limited to 60 frames per second, at a resolution of 1980×1080 pixel², the system is unable to capture the inner mechanisms of the vortices seen, closer to the centre of the vortices. This may lead to an error in calculation of peak vorticity. While zooming in would resolve this issue, it would be at the expense of overall picture and increase the particle size.

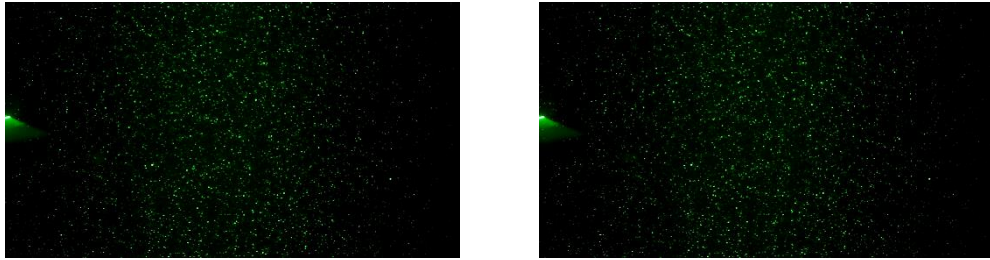


Figure 4.1: Sample consecutive images before processing. The area with the hydrofoil is masked while processing.

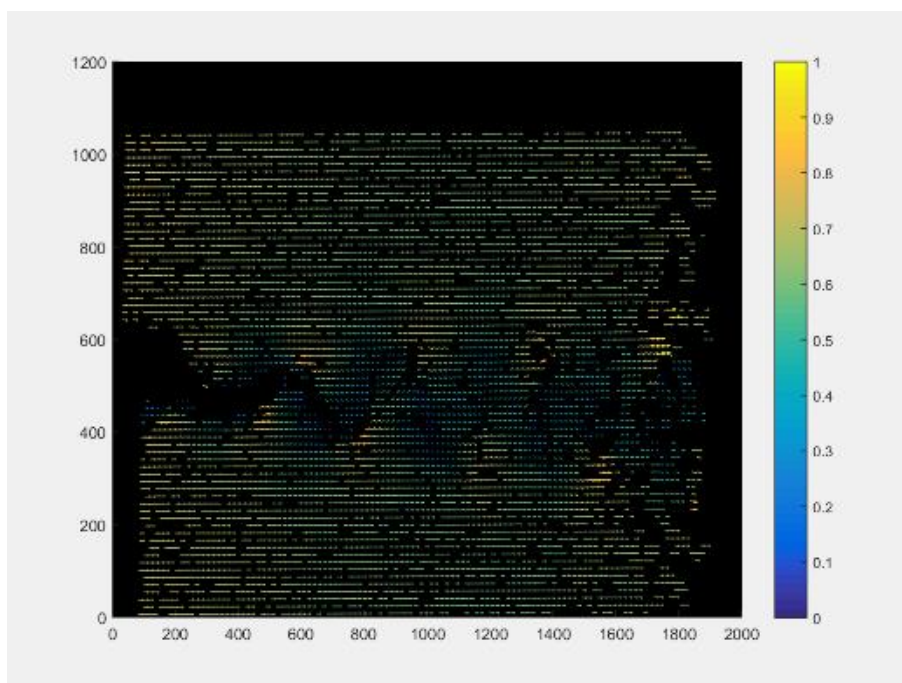


Figure 4.2: Velocity profile for consecutive images shown in Figure 4.1 without interpolation

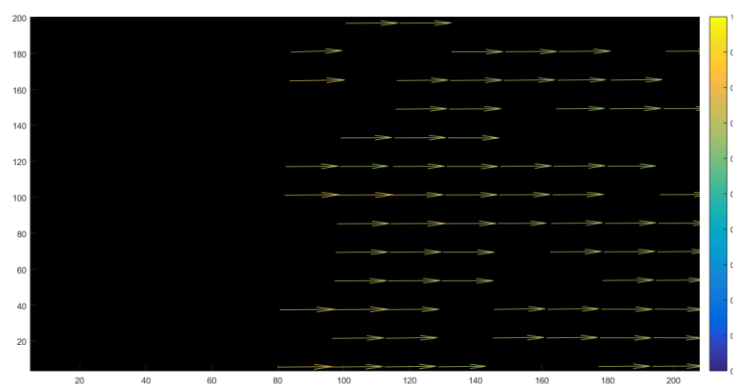


Figure 4.3: Velocity profile for consecutive images shown in Figure 4.1 without interpolation - zoomed in

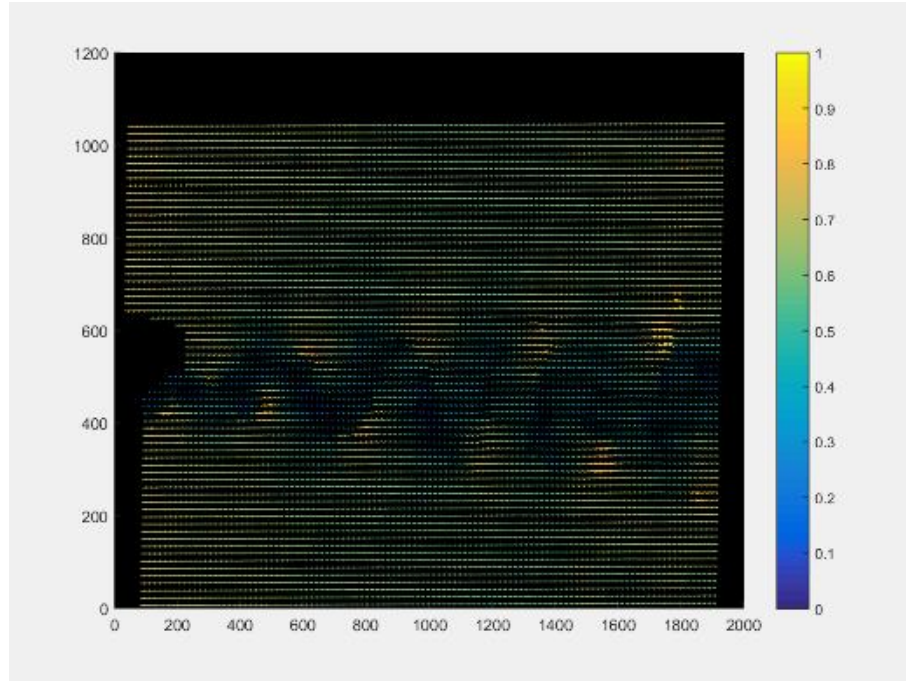


Figure 4.4: Velocity profile for consecutive images shown in Figure 4.1

The velocity vectors shown here allow the option to normalize each value with the maximum value observed for the given pair of images. The units for x and y axis are pixels.

While the current tests results show accurate results, this is a problem at higher speeds.

However, as this is restricted to points near the centre of the vortex, the outer areas of the vortex remain easily observable.

The figures above show a sample result for the PIV system. They also illustrate that the fact that the particles need not be visible to the naked eye, and that the interpolation algorithms used in the code are effective.

Attempts were made to use this system to quantify the flow near the flow near the pitching hydrofoil, but the required pixel resolution was not obtained due to the limitation posed by the speed of the camera.

4.2 System advantages and limitations

Listed below are the advantages and limitations of the system developed in this thesis when compared to a conventional commercially available PIV system.

The advantages:

1. It allows easy control over the focus of the experiment, allowing the modification of area of interest as required (illuminated area, distance from object of interest, focus, etc.)
2. It is highly portable, allowing the user to perform experiments in multiple scenarios as required
3. It can be used under water by sealing in the laser
4. The code has an inbuilt ability to mask out areas which are not of interest improving the speed of computation
5. It is one of the least expensive setups, costing a little under \$3000 (USD)
6. The code allows control over progressive interrogation window size, to get more precise results by careful selection of the lowest interrogation window size
7. The code allows multiple procedures for cross correlation (methods of calculation of Fast Fourier Transform) as well as filters. It also allows for user defined image processing to gain the best possible results

Limitations:

1. The speed of the camera limits the speed of flow. Since the best DSLR cameras currently have a maximum speed of 60 frames/second, the system is restricted by this constraint. The effects of this are seen when the area around a pitching foil is considered
2. This type of setup uses a cylindrical concave lens to spread the laser beam into a plane; the code used to process the images is also restricted to 2D.
3. While some systems allow the user to observe both sides of the object of interest, the setup in its current form allows viewing of only one side of the object. The use of mirrors to light up the object of interest from other directions leads to a loss of light intensity as well as spreading of the beam in a direction perpendicular to the plane
4. The masking feature in the code only allows for a stationary mask. Having a mask that undergoes predefined motions linked to frames would increase the usage of this method

Chapter 5: Conclusions and Discussion

Presented here are the results of experiments aimed at determining the performance of two quasi-two-dimensional hydrofoils arranged in an in-line configuration. This study aims at understanding the role of pitching motion of a caudal fin in the presence of a dorsal fin, decoupled from heaving motion. The net thrust generated (and efficiency, under acceleration conditions) or free swimming speed, the work done, and economy of the double foil configuration were measure directly using a custom build test rig assembly and water flow tank.

The experiments focus on four parameters; distance of separation, frequency, amplitude, and flexibility of the hydrofoils. The following conclusions are drawn:

1. During acceleration
 - a. higher frequencies and amplitudes show increased efficiencies for the double hydrofoil configuration as compared to the single hydrofoil configurations
 - b. the effect of the leading hydrofoil on work done during movement of the lagging hydrofoil reduces with increasing distance of separation
2. During free swimming with rigid hydrofoils
 - a. the effect of the leading hydrofoil on free swimming speed reduces as the magnitude of free swimming speed increases
 - b. the effect of the leading hydrofoil on work done during movement of the lagging hydrofoil is greater at higher speeds
 - c. the effect of the leading hydrofoil on work done during movement of the lagging hydrofoil is lower with increasing distance of separation

- d. the double hydrofoil configuration consistently shows greater values for economy than the single foil configuration for the same input parameters (frequency, amplitude and distance of separation)
 - e. the double hydrofoil configuration consistently shows reductions in the value of economy for increasing distance of separation for the same input parameters (frequency and amplitude)
3. Flexible foils
- a. are more efficient than rigid foils for a single hydrofoil configuration; rigid hydrofoils show much greater increases of economy (in terms of a percentage) than flexible hydrofoils when in double hydrofoil configuration.
 - b. are show greater values of economy for the double hydrofoil configuration as compared to the single hydrofoil configuration only for larger frequencies and amplitudes
 - c. the double hydrofoil configuration consistently shows reductions in the value of economy with increasing distance of separation for the same input parameters

The results clearly show that the benefit of a static dorsal fin go beyond simple stabilization. While the presence of the dorsal fin does cause a small reduction in net thrust and free swimming speed, it ensures lower energy consumption per unit distance travelled. This leads to the conclusion that the addition of a dorsal fin or hydrofoil is beneficial for reducing energy consumption.

The only exceptions occur during acceleration at low frequencies and amplitudes of oscillation, a condition not observed in nature.

The main reason for the increase in efficiency is the change in work done by the lagging hydrofoil while undergoing pitching motions. As the results show, the thrust values for the experiments under acceleration conditions and the free-swimming speed values for the experiments under free swimming conditions for the double hydrofoil configuration are lower than their corresponding single hydrofoil configuration values, which, in and of itself, causes reductions in the values of efficiency and economy respectively.

This reduction in work done is due to the reduced speed of flow, not due to any interaction between the vortices shed by the stationary and pitching hydrofoil for the following reasons:

1. The experiments were carried out without matching the pitching frequency of the lagging hydrofoil with the frequency of vortex shedding from the stationary hydrofoil
2. The values for work done and thrust and time averaged
3. Experiments were performed a minimum of three times (on average, five times) wherein the pitching was started without regard to the position of the closest oncoming vortex, which once again averages out any specific vortex interaction. This was confirmed using PIV.

Presented below is the time averaged flow velocity behind the stationary hydrofoil. The speed of flow is 14.5 cm/s. Here the flow at each point of interest is recorded and averaged over time. The grid spacing chosen here is 32 pixels x 32 pixels which is 0.74 cm x 0.74 cm. The area under consideration is approximately 45 cm x 25 cm, with extremities masked to reduce computation time.

It shows that the flow immediately behind the hydrofoil is significantly slower as compared to the speed of oncoming flow and that the flow behind the stationary hydrofoil regains some of

its lost momentum as the distance from the stationary hydrofoil increases. This also supports the conclusion that the effect of the presence of the stationary hydrofoil on work done reduces with increased distance of separation.

The velocity vectors showing the direction of mean flow are normalized in magnitude, while the magnitude of velocity diagram (Figure 5.2) is in cm/s. Sample raw images and velocity profiles for a pair of images within the time period considered are also shown.

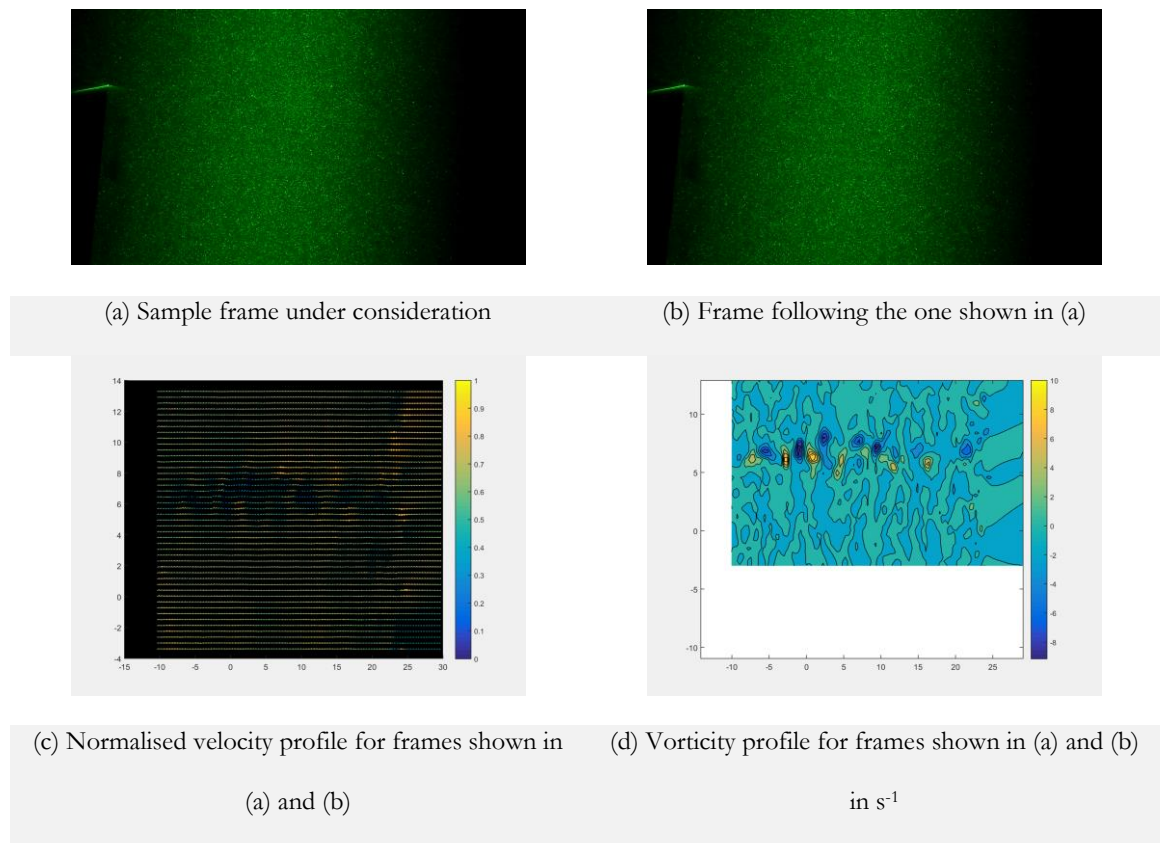


Figure 5.1: Samples images under consideration

Figure 5.2: Time averaged magnitude of velocity of flow behind the stationary hydrofoil. Both axes are in cm. The colour bar shows the magnitude of velocity in cm/s. Figure 5.3 shows the time averaged velocity profile at the distances of separation chosen for the aforementioned experiment sets (2C, 2.5C and 3C). As can be seen the velocity immediately behind the stationary hydrofoil is lower than the speed of oncoming flow and increases with increased distance of separation. A similar pattern is seen at other speeds considered in the experimental sets.

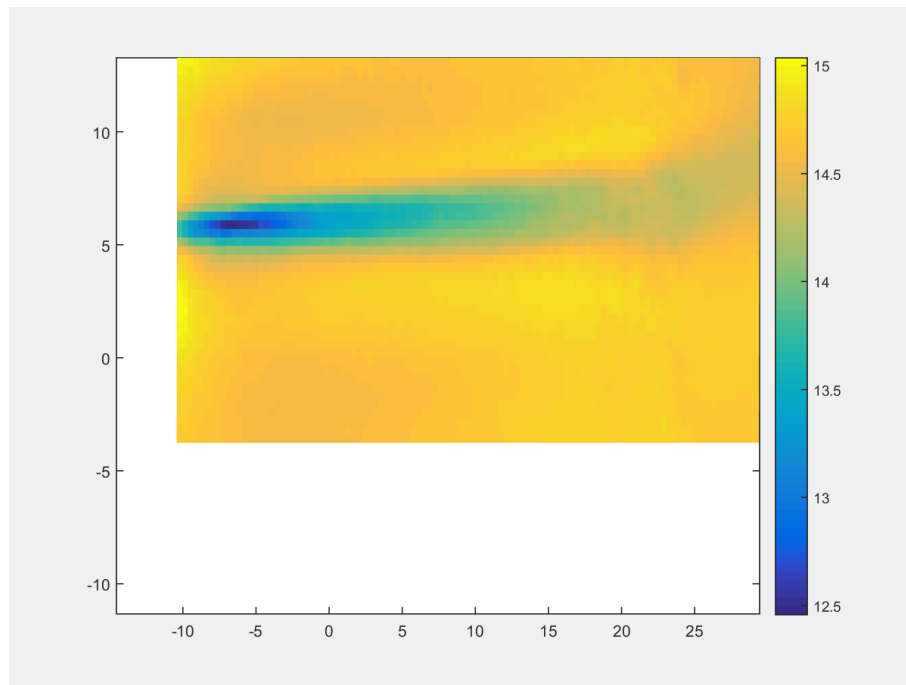


Figure 5.2: Time averaged magnitude of velocity of flow behind the stationary hydrofoil. Both axes are in cm. The colour bar shows the magnitude of velocity in cm/s.

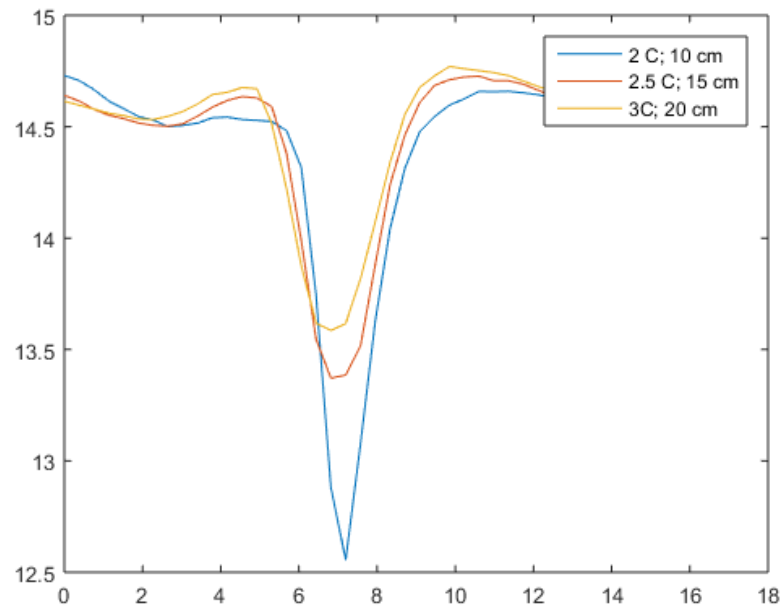


Figure 5.3: Cross-sectional time averaged velocity profile of flow at a given distance behind the stationary hydrofoil. The x axis represents distance perpendicular to the flow direction.

These results differ from the ones in [57]. In the experiments presented in [57], both the hydrofoils in the inline configuration are pitching, while in the work presented here, the leading hydrofoil is stationary. This leads to 2 major differences:

1. The vortices shed by the leading hydrofoil in [57] are significantly greater in strength as compared to the ones shed by the leading hydrofoil in the aforementioned experimental sets
2. The vortices shed by the leading hydrofoil in [57] produce a reverse von Karman vortex street and lead to an increased time averaged speed of flow behind the hydrofoil, while the ones produced by the stationary hydrofoil in the experimental sets

described in this work produce a von Karman vortex street which reduces the time averaged speed of flow behind the hydrofoil

Finally, [57] explores the effect of the interaction between the vortices created by the leading and trailing hydrofoils. The vortex shedding from the leading hydrofoil is controlled by the pitching motion of the leading hydrofoil; the phase difference between the pitching motion of the hydrofoils controls the interaction between the vortices shed. It is this interaction that leads to changes in thrust, work done and economy; their increase or decrease is a function of phase difference.

In the work presented here, the vortex shedding from the stationary hydrofoil is passive and the effect of any interaction between the vortices shed by both the hydrofoils is averaged out.

Chapter 6: Future Work

Since this is a simplified model, additional complexity in terms of movement can be added to it. Further studies can be devoted to:

1. Understanding the correlation of shape and size of the leading hydrofoil with these benefits.

The current study, leaning toward bio-inspiration uses a larger dorsal fin, relative to the size of the corresponding caudal fin, than seen in nature. Generally, the dorsal fin is the shape and size of half the caudal fin. This also allows the effects of the presence of the dorsal fin to be magnified. Hence changing the shape and size will affect the effects of its presence on all the parameters considered.

2. The effect of flexibility of the leading hydrofoil.

The current study assumes a rigid hydrofoil. While there have been studies involving flexible fins, the fins are ribbed and tend to pulse. A simpler model with a flexible foil that simply responds to the movement of the entire configuration during pitching could be studied to isolate any effects of interest.

3. Heaving motion can be added to this model

Since this is a simplified model, specifically created to decouple the effects of heaving and pitching, heaving motion could be added to the configuration. This would increase the lateral forces on the dorsal foil causing it to move passively. The effects of a flexible dorsal foil compared to a rigid dorsal foil under these conditions would be of particular interest.

4. Addition of minor flippers at angles to the foil could have interesting hydrodynamic and control effects.

This would move the study in the direction of creating bio-inspired robotic fish. It would be easier to decouple their effects from the overall fish and study them in isolation. Their addition would move the experiment out of the 2D plane into 3D space allowing for increased response to flow conditions.

Chapter 7: Bibliography

- [1] C. Breder, "The locomotion of fishes," *Zoologica*, vol. 4, pp. 159-297, 1926.
- [2] R. Alexander, *Functional design in fishes*, Hutchinson, London, 1967.
- [3] J. Gray, "Studies in Animal Locomotion," *Journal of Experimental Biology*, 1936.
- [4] C. Wardle, J. J. Videler and J. D. Altringham, "Review tuning into fish swimming waves: body form, swimming mode and muscle function," *The Journal of Experimental Biology*, pp. 198, 1629–1636, 1995.
- [5] J. Gray, *Animal Locomotion.*, 1968.
- [6] Y. Aleyev, 1977.
- [7] R. Blake, *Fish Locomotion*, Cambridge: Cambridge Univ. Press, 1983.
- [8] J. Anderson, *Vortex control for efficient propulsion*, Cmpbridge, MA, 1996.
- [9] S. Sane and M. Dickinson, "The control and flight force by flapping wing: lift and drag production," *Journal of Experimental Biology*, 2001.
- [10] E. Stamhuis and J. Videler, "Stamhuis E, Videler J. 1995. Quantitative flow analysis around aquatic animals using laser sheet particle image velocimetry," *Journal of Experimental Biology*, vol. 198, pp. 283-294, 1995.
- [11] U. Muller, B. van den Heuvel, E. Stamhuis, J. Videler and e. al., "Fish foot prints: morphology and energetics of the wake behind a continuously swimming mullet (*Chelon labrosus risso*)," *Journal of Experimental Biology*, p. 57:673–93, 1997.
- [12] M. Wolfgang, J. Anderson, M. Grosenbaugh, D. Yue and M. Triantafyllou, "Near-body flow dynamics in swimming fish," *Journal of Experimental Biology*, p. 202:2303–27, 1999.
- [13] J. Liao, D. Beal, G. Lauder and M. Triantafyllou, "The Kármán gait: novel body kinematics of rainbow trout swimming in a vortex street," *Journal of Experimental Biology*, pp. 206: 1059-1073, 2003.
- [14] R. E.Shadwck, "How Tunas and Lamnid Sharks Swim: An evolutionary Convergence," *American Scientist*, November 2005.

- [15] J. Donley, C. Sepulveda, P. Konstantinidis, S. Gemballa and R. Shadwick, "Convergent evolution in mechanical design of lamnid sharks and tunas," *Nature*, vol. 429, pp. 61-65, 2004.
- [16] F. Fish and G. Lauder, "Passive and active flow control by swimming fishes and mammals," *Annual Review of Fluid Mechanics*, vol. 38, pp. 193-224, 2006.
- [17] G. Triantafyllou, M. Triantafyllou and M. Grosenbaugh, "Optimal thrust development in oscillating foils with application to Fish Propulsion," *J. Fluids Struct.*, p. 7:205-24, 1993.
- [18] P. Liu and N. Bose, "Propulsive thrust of an oscillating foil at large angles of attack: experimental study," *Am. Towing Tank Conf.*, p. 453:1763-70, 1997.
- [19] B. Ahlborn, S. Chapman, R. Stafford, R. Blake and D. Harper, "Experimental simulation of the thrust phases of fast-start swimming of fish," *J. Theor. Biol.*, p. 200:2301-12, 1997.
- [20] B. Ahlborn, D. Harper, R. Blake, D. Ahlborn and M. Cam, "Fish without footprints," *J. Theor. Biol.*, pp. 148:521-33, 1991.
- [21] E. Drucker and G. Lauder, "Locomotor function of the dorsal fin in rainbow trout: kinematic patterns and hydrodynamic forces," *J Exp Biol.*, pp. 208(Pt 23):4479-94., 2005.
- [22] E. Drucker and G. Lauder, "Wake dynamics and fluid forces of turning maneuvers in sunfish," *J Exp Biol.*, pp. Feb;204(Pt 3):431-42, 2001.
- [23] E. M. Standen and G. Lauder, "Dorsal and anal fin function in bluegill sunfish *Lepomis macrochirus*," *The Journal of Experimental Biology*, pp. 208, 2753-2763, 2005.
- [24] E. Drucker and G. Lauder, "Locomotor function of the dorsal fin in teleost fishes: experimental analysis of wake forces in the sunfish," *The Journal of Experimental Biology*, 2001.
- [25] M. Rosen, *Water flow about a swimming fish*, Los Angeles: University of California in Los Angeles, 1959.
- [26] G. Aleyev, *Nekton*, 1997.
- [27] J. Liao, D. Beal, G. Lauder and M. Triantafyllou, "Fish Exploiting Vortices Decrease Muscle Activity," *Science*, vol. 302, pp. 1566-1569, 2003.
- [28] D. Ames, *Shear Flow Visualization at High Reynolds Numbers*, Massachusetts Institute of Technology, 1998.

- [29] P. Tokomaru and P. Dimotakis, "Rotary oscillation control of a cylinder wake," *J. Fluid Mech.*, p. 224:77–90, 1991.
- [30] L. Cortelezzi, "Nonlinear feedback control of the wake past a plate with a suction point on the downstream wall," *J. Fluid Mech.*, p. 327:303–324, 1996.
- [31] P. Koumoutsakos, "Vorticity flux control for a turbulent channel flow," *Phys. Fluids*, p. 11:248–250, 1999.
- [32] D. Rockwell, "Vortex-body interactions," *Annu. Rev. Fluid Mech.*, p. 30:199–229, 1998.
- [33] I. Gursul and C. Ho, "High aerodynamic loads on an airfoil submerged in an unsteady stream," *Am. Inst. Aeronaut. Astronaut. J.*, p. 30:1117–19, 1992.
- [34] K. Hoppe, "The dynamo-elastic oscillating foil propeller," *Schiff Hafen*, p. 5:54–61, 1989.
- [35] J. Anderson, K. Streitlien, D. Barrett and M. Triantafyllou, "Oscillating foils of high propulsive efficiency," *J. Fluid Mech.*, p. 360:41–72, 1998.
- [36] M. Koochesfahani and P. Dimotakis, "A cancellation experiment in a forced turbulent shear layer," *Am. Inst. Aeronaut. Astronaut. Tech.*, pp. 88-3713-CP, 1988.
- [37] L. Cortelezzi, Y.-C. Chen and H.-L. Chang, "Nonlinear feedback control of the wake past a plate: from a low-order model to a higher-order model," *Phys. Fluids*, p. 9(7):2009–22, 1997.
- [38] M. Triantafyllou, G. Triantafyllou and R. Gopalkrishnan, "Wake mechanics for thrust generation in oscillating foils," *Phys. Fluids*, p. A 3:2835–37, 1991.
- [39] T. Wu, "Hydromechanics of swimming propulsion. Part 1. Swimming of a two dimensional flexible plate at variable forward speeds in an inviscid fluid," *J. Fluid Mech.*, p. 46:337–55, 1971a.
- [40] T. Wu, "Swimming of a waving plate," *J. Fluid Mech.*, p. 10:321–44, 1961.
- [41] T. Wu, "Hydromechanics of swimming fishes and cetaceans," *Adv. Appl. Mathe.*, p. 11:1–63, 1971b.
- [42] M. Lighthill, "Note on the swimming of slender fish," *J. Fluid Mech.*, p. 9:305–17, 1960.
- [43] M. Lighthill, "Aquatic animal propulsion of high hydromechanical efficiency," *J. Fluid Mech.*, p. 44:265–301, 1970.
- [44] M. Wolfgang, M. Triantafyllou and D. Yue, "Visualization of complex near-body transport processes in flexible-body propulsion," *J. Visual.*, no. 2(2), In press, 1999b.

- [45] D. Read, F. Hover and M. Triantafyllou, “Forces on oscillating foils for propulsion and maneuvering,” *Journal of Fluids and Structures*, vol. 17, no. 1, pp. 163-183, 2003.
- [46] F. Hover, Ø. Haugsdal and M. Triantafyllou, “Effect of angle of attack profiles in flapping foil propulsion,” *Journal of Fluids and Structures*, vol. 19, no. 1, pp. 37-47, 2004.
- [47] G. Lauder, E. Anderson, J. Tangorra and Madden PGA, “Fish biorobotics: kinematics and hydrodynamics of self-propulsion,” *Journal of Experimental Biology*, pp. 210: 2767-2780, 2007.
- [48] S. Licht, M. Wibawa, F. Hover and M. Triantafyllou, “In-line motion causes high thrust and efficiency in flapping foils that use power downstroke,” *J Exp Biol.*, vol. 213, no. 1, pp. 63-71, 2010 .
- [49] J. Liu, I. Dukes and H. Hu, “Novel Mechatronics Design for a Robotic Fish,” in *IEEE/RSJ International Conference on Intelligent Robots and Systems*, 2005.
- [50] J. Anderson and N. Chhabra, “Maneuvering and Stability Performance of a Robotic Tuna,” *Integ. and Comp. Biol.*, no. 42, p. 118–126, 2002.
- [51] J. Long Jr and e. al., “Four flippers or two? Tetrapodal swimming with an aquatic robot,” *Bioinspiration and Biomimetics*, no. 1, pp. 20-29, 2006.
- [52] R. Clark and A. Smits, “Thrust production and wake structure of a batoid-inspired oscillating fin,” *J. Fluid Mech.*, vol. 562, pp. 415-429, 2006.
- [53] S. Alben, C. Witt, T. Baker, E. Anderson and G. Lauder, “Dynamics of freely swimming flexible foils,” *Phys. Fluids*, 2012.
- [54] G. Lauder, B. Flammang and S. Alben, “Passive Robotic Models of Propulsion by the Bodies and Caudal,” *Integrative and Comparative Biology*, vol. 52, no. 5, pp. 576-587, 2012.
- [55] P. Dewey, B. Boschitsch, K. Moored, H. Stone and A. Smits, “Scaling laws for the thrust production of flexible pitching panels,” *Journal of Fluid Mechanics*, vol. 732, pp. 29-46, 2013.
- [56] G. Triantafyllou, M. Triantafyllou and M. Grosenbaugh, “Optimal Thrust Development in Oscillating Foils with Application to Fish Propulsion,” *Journal of Fluids and Structures*, vol. 7, no. 2, pp. 205-224, 1993.
- [57] B. Boschitsch, P. Dewey and A. Smits, “Propulsive performance of unsteady tandem hydrofoils in an in-line configuration,” *Physics of Fluids*, vol. 26, no. 5, 2014.
- [58] P. Dewey, D. Quinn, B. Boschitsch and A. Smits, “Propulsive performance of unsteady tandem hydrofoils in a side-by-side configuration,” *Physics of Fluids*, 2014.

- [59] M. Reidenbach, N. George and M. Koehl, “Antennule morphology and flicking kinematics facilitate odor sampling by the spiny lobster, *Panulirus argus*,” *Journal of Experimental Biology*, 2008.
- [60] E. Cowen and S. Monismith, “A hybrid digital particle tracking velocimetry technique,” *Experiments in Fluids*, vol. 22, no. 3, pp. 199-211, 1997.
- [61] J. Stocking, J. Rippe and M. Reidenbach, “Structure and dynamics of turbulent boundary layer flow over healthy and algae-covered corals,” *Coral Reefs (2016)*, p. 35:1047–1059, 2016.
- [62] M. Koehl and M. Reidenbach, “Swimming by microscopic organisms in ambient water flow,” *Experiments in Fluids*, vol. 43, no. 5, pp. 755-768, 2007.
- [63] S. Pravin and M. Reidenbach, “Simultaneous Sampling of Flow and Odorants by Crustaceans can Aid Searches within a Turbulent Plume,” *Sensors*, 2013.
- [64] O. Williams and A. Smits, “Application of PIV to the Measurement of Hypersonic Turbulence,” in *16th Int Symp on Applications of Laser Techniques to Fluid Mechanics*, Lisbon, Portugal, 2012.
- [65] R. H. R. Corporation, *RHRC Research Water Tunnels*.
- [66] F. Marey, *Le Mouvement*, 1884.
- [67] A. Megnan, *Ann. Sci. nat.*, vol. 13, 1930.
- [68] J. Gray, *Journal of Experimental Biology*, vol. 10, 1993.
- [69] J. Sveen, *An introduction to MatPIV v. 1.6.1*, Oslo, 2004.
- [70] M. Triantafyllou, D. Barrett, D. Yue, J. Anderson, M. Grosenbaugh and e. al., “A new paradigm of propulsion and maneuvering for marine vehicles,” *Trans. Soc. Naval Architects Marine Eng.*, pp. 104:81-100, 1996.
- [71] F. Fish, L. Howle and M. Murray, “Hydrodynamic flow control in marine mammals,” *Integrative and Comparative Biology*, pp. 788-800, 2008.
- [72] R. Gopalkrishnan, M. Triantafyllou, G. Triantafyllou and D. Barrett, “Active vorticity control in a shear flow using a flapping foil,” *J. Fluid Mech*, p. 274:1–21, 1994.
- [73] J. Buchholz and A. Smits, “On the evolution of the wake structure produced by a low-aspect-ratio pitching panel,” *Journal of fluid mechanics*, pp. 433-443, 2006.
- [74] J. Gray, *How animals move*, Cambridge University Press, Cambridge, 1953.
- [75] J. Gray, *Animal locomotion*, Weidenfeld and Nicolson, London, 1968.

- [76] R. Gonzales and R. Woods, Digital Image Processing, Addison-Wesley, 1992.
- [77] R. Keane and R. Adrian, "Theory of cross-correlation analysis of piv images," *Applied Scientific Research*, no. 49, pp. 191-215, 1992.
- [78] M. Raffel, C. Willert and J. Kompenhans, Particle Image Velocimetry, A Practical Guide., Springer, 1998.
- [79] S. K., G. Triantafyllou and M. Triantafyllou, "Efficient foil propulsion through vortex," *AIAA J*, vol. 34, no. 23, pp. 15-19, 1996.
- [80] P. Bandyopadhyay, "Trends in Biorobotic Autonomous Undersea Vehicles," *IEEE Journal of Oceanic Engineering*, vol. 30, no. 1, pp. 109-139, 2005.
- [81] S. Davidson, I. Hunter, P. Madden and G. Lauder, "The Development of a Biologically Inspired Propulsor for Unmanned Underwater Vehicles," *IEEE Journal of Oceanic Engineering*, vol. 32, no. 3, pp. 533-550, 2007.
- [82] M. Triantafyllou and G. Triantafyllou, "An Efficient Swimming Machine," *Scientific American*, vol. 272, no. 3, pp. 64-70, 1995.